

## RESEARCH ARTICLE

10.1029/2018JF004720

## Key Points:

- Meteoric beryllium-10 is used to generate point-based estimates of long-term erosion on paired hillslopes
- These estimates suggest that erosion rates have increased by 2 orders of magnitude under agricultural management
- Model choice influences erosion rate magnitude, but average rates are similar to estimates from process-based models and cesium-137

## Supporting Information:

- Supporting Information S1
- Movie S1
- Movie S2

## Correspondence to:

N. A. Jelinski,  
jeli0026@umn.edu

## Citation:

Jelinski, N. A., Campforts, B., Willenbring, J. K., Schumacher, T. E., Li, S., Lobb, D. A., et al. (2019). Meteoric beryllium-10 as a tracer of erosion due to postsettlement land use in west-Central Minnesota, USA. *Journal of Geophysical Research: Earth Surface*, 124, 874–901. <https://doi.org/10.1029/2018JF004720>

Received 21 APR 2018

Accepted 18 FEB 2019

Accepted article online 20 FEB 2019

Published online 2 APR 2019

## Meteoric Beryllium-10 as a Tracer of Erosion Due to Postsettlement Land Use in West-Central Minnesota, USA

Nicolas A. Jelinski<sup>1</sup> , Benjamin Campforts<sup>2</sup> , Jane K. Willenbring<sup>3</sup>, Thomas E. Schumacher<sup>4</sup>, Sheng Li<sup>5</sup>, David A. Lobb<sup>6</sup>, Sharon K. Papiernik<sup>7</sup>, and Kyungsoo Yoo<sup>1</sup>

<sup>1</sup>Department of Soil, Water and Climate, University of Minnesota Twin-Cities, Saint Paul, MN, USA, <sup>2</sup>Department of Earth and Environmental Sciences, KU Leuven, Heverlee, Belgium, <sup>3</sup>Scripps Institution of Oceanography, University of California-San Diego, La Jolla, CA, USA, <sup>4</sup>Department of Plant Science, South Dakota State University, Brookings, SD, USA, <sup>5</sup>Agriculture and Agri-Food Canada, Fredericton, New Brunswick, Canada, <sup>6</sup>Department of Soil Science, University of Manitoba, Winnipeg, Manitoba, Canada, <sup>7</sup>North Central Agricultural Research Laboratory, USDA-ARS, Brookings, SD, USA

**Abstract** Meteoric beryllium-10 ( $^{10}\text{Be}_m$ ,  $t^{1/2} = 1.4$  Myr) is a cosmogenic radionuclide that remains largely underutilized for deriving hillslope-scale estimates of erosion on uplands under conditions of land use change. We applied two different models for estimating erosion rates from observed  $^{10}\text{Be}_m$  concentrations (a one-dimensional model predicting vertical profiles of  $^{10}\text{Be}_m$  within hillslope soils [loss only, diffusion only, LODO] and a two-dimensional model predicting the concurrent evolution of hillslope topography and  $^{10}\text{Be}_m$  distributions via bioturbation, chemical mobility, and surface erosion [Be2D]). Both models were used to derive pre-European and post-European settlement erosion rates ( $E_{\text{nat}}$  and  $E_{\text{post}}$ , respectively) across paired cultivated and uncultivated hillslopes in west-central Minnesota, USA.  $E_{\text{post}}$  estimates from  $^{10}\text{Be}_m$  were compared to  $E_{\text{post}}$  estimates derived from  $^{137}\text{Cs}$  inventories and the process-based Water and Tillage Erosion Model (WaTEM). The results from these models suggest that erosion rates from upper positions on the cultivated hillslope have increased from an average of 0.047 mm/year under natural conditions to  $E_{\text{post}}$  values of 3.09 mm/year. The Be2D and LODO models, on average, produced  $E_{\text{post}}$  estimates that were similar in magnitude to WaTEM and  $^{137}\text{Cs}$  conversion models. This numerical convergence does not imply absolute  $^{10}\text{Be}_m$  model accuracy, particularly when considering the uncertainties inherent in each approach, but it does suggest that the orders of magnitude increase in estimated erosion rates from  $E_{\text{nat}}$  to  $E_{\text{post}}$  is robust. Additionally, the pattern of  $E_{\text{post}}$  estimates produced using  $^{10}\text{Be}_m$  conversion models is supported by the distribution of soil inorganic carbon at the study site. Our results demonstrate that  $^{10}\text{Be}_m$  can provide reasonable estimates of both predisturbance and postdisturbance erosion rates in landscapes that have undergone extensive human modification.

**Plain Language Summary** Agricultural practices have substantially changed soil erosion rates in the Midwestern United States. Although much work has been devoted to understanding the changes in soil erosion rates with land cover change, the ability to quantify those changes at discrete locations on the landscape over long periods of time has been limited. We use a set of tracers and models to estimate presettlement and postsettlement erosion rates on a hillslope in west-central Minnesota, USA, and show that soil erosion has increased by approximately 1 to 2 orders of magnitude over a period of approximately 110 years. This has implications for how we view our current agricultural landscapes and how we think about soil sustainability in the future.

### 1. Introduction

Beryllium-10 ( $^{10}\text{Be}$ ) is a cosmogenic radionuclide with a half-life of 1.4 million years (Chmeleff et al., 2010; Korschinek et al., 2009; Nishiizumi et al., 2007) that is produced when high-energy cosmic radiation strikes oxygen and nitrogen atoms, resulting in spallation (Dunai, 2010). Beryllium-10 produced through spallation reactions in solid substances at Earth's surface (commonly referred to as in situ beryllium-10 [ $^{10}\text{Be}_i$ ]) occupies sites in mineral matrices. In contrast,  $^{10}\text{Be}$  produced through spallation reactions in the atmosphere, commonly referred to as *meteoric* beryllium-10 ( $^{10}\text{Be}_m$ ), is rapidly adsorbed onto aerosols following

production and falls out to Earth's surface in both wet and dry deposition (Nishiizumi et al., 2007; Willenbring & von Blanckenburg, 2010).

$^{10}\text{Be}_m$ , due to its widespread distribution and long half-life, has been used to quantify (1) long-term erosion and soil production rates under natural vegetation on steady state landscapes (Bacon et al., 2012; Johnson et al., 2014; Monaghan et al., 1992; Pavich et al., 1986; Schoonejans et al., 2017), (2) surface ages (Graly et al., 2010; Pavich et al., 1985; Tsai et al., 2008), (3) global rates of mineral weathering (Willenbring & von Blanckenburg, 2010), (4) loess accumulation rates (Harden et al., 2002), (5) basin-wide erosion or denudation rate averages (Brown et al., 1988; von Blanckenburg et al., 2012; Rahaman et al., 2017; Wittmann et al., 2015; Wittman & von Blanckenburg, 2016), (6) sediment movement (Portenga et al., 2017; Reusser & Bierman, 2010), and (7) the fate of regolith under the influence of glacial processes (Balco, 2004; Ebert et al., 2012). Although the use of  $^{10}\text{Be}$  as a tracer of erosion and landscape change due to human disturbance has been suggested for several decades (Harden et al., 2002; Lal, 1991), the quantitative utility of  $^{10}\text{Be}_m$  to produce estimates of changes in erosion rates at discrete locations on the landscape due to agricultural management has only received cursory exploration (Graly et al., 2010; Harden et al., 2002). Emerging spatially explicit numerical models for  $^{10}\text{Be}_m$ , such as the Be2D model (Campforts et al., 2016), can produce estimates of erosion rates in nonsteady state landscapes under both natural conditions and human disturbance and provide novel opportunities to evaluate the effects of land use on erosion rates.

Understanding changes in erosion rates in regions dominated by agricultural land use is critical for predicting the future sustainability of soils for agronomic and environmental purposes (Lal & Stewart, 2012). In the U.S. Corn Belt region (comprising portions of the states of Iowa, Illinois, Indiana, Nebraska, and Minnesota), the conversion of much of the landscape from natural vegetation to agricultural lands occurred largely over the time period 1850–1930 CE (Ramankutty & Foley, 1999) as a result of European settlement and homesteading activities. Due to well-constrained land use histories, the rapid pace of land use change following European settlement, and the agronomic importance of the Corn Belt, this region provides an excellent context for the application of  $^{10}\text{Be}_m$  in agricultural landscapes.

The purpose of this work was to use  $^{10}\text{Be}_m$  to derive spatially explicit pre-European and post-European settlement erosion rates across a hillslope currently under agricultural land use. To contextualize and further test our findings, we also examined soil morphological characteristics, the distribution of soil constituents potentially impacted by erosion (such as organic and inorganic carbon), and erosion rates predicted from a short-lived radionuclide ( $^{137}\text{Cs}$ ,  $t^{1/2} = 30.17$  years) and a process-based soil erosion model (Water and Tillage Erosion Model [WaTEM]; van Oost et al., 2000). Our specific objectives were to (1) investigate the distribution of  $^{10}\text{Be}_m$ ,  $^{137}\text{Cs}$ , and soil organic and inorganic carbon across paired cultivated and uncultivated hillslopes in west-central Minnesota, USA; (2) derive location-specific estimates of natural and postsettlement ( $E_{\text{nat}}$  and  $E_{\text{post}}$ , respectively) erosion rates using two different  $^{10}\text{Be}_m$  conversion models (which convert observations of radionuclide distributions into quantitative erosion rates); and (3) compare the results of these models to erosion rate estimates from  $^{137}\text{Cs}$  conversion models and the WaTEM model (a process-based model, which estimates tillage and water erosion; van Oost et al., 2000), applied to these same sampling locations. Finally, we consider the potential opportunities and challenges facing the use of  $^{10}\text{Be}_m$  at our study site and in other agricultural settings around the world.

## 2. Materials and Methods

### 2.1. Study Area

#### 2.1.1. Glacial Geology and Soils

The study area consists of paired uncultivated and cultivated hillslopes in west-central Minnesota, USA, approximately 7 km north of the town of Cyrus, in Pope County ( $-95.74^\circ\text{W}$ ,  $45.67^\circ\text{N}$ ; Figure 1). These hillslopes lie on the margins of the Alexandria moraine complex—a landscape which was initially formed by the Wadena Lobe of the southern Laurentide Ice Sheet and eventually overridden (in part) by the Des Moines Lobe during its southeasterly advance in the later stages of the Wisconsinan glaciation (Wright, 1962). Surficial sediments in the study area are composed of glacial till of the Goose River formation on the uplands, with Quaternary and Holocene alluvial sediments in the river valleys (Harris, 2003). Goose River group sediments are loamy-textured, carbonate-rich Wisconsin-age glacial tills of the Des Moines lobe (Harris, 2003). Detailed analyses of buried organic sediments and optically stimulated luminescence on

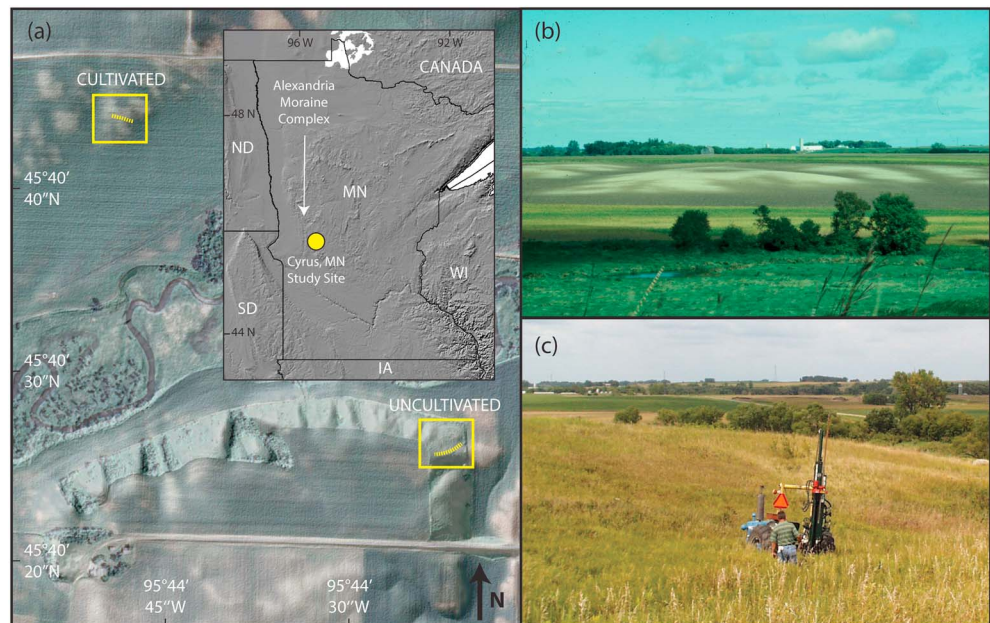


**Figure 1.** Study site landscape setting and hillslope transects. (a) Regional setting (inset), orthophoto and hillshade of study site showing location of cultivated and uncultivated sampling areas. U.S. state abbreviations represent Iowa (IA), Minnesota (MN), North Dakota (ND), SD (South Dakota), and Wisconsin (WI). The yellow dotted lines show hillslope transect locations. (b) Landscape photo of cultivated transect with eroded summit, shoulder, and backslopes (light-colored, exposed subsurface material). Photo Credit: S. K. Papiernik. (c) Landscape photo of uncultivated hillslope. Photo Credit: T.E. Schumacher.

quartz grains have constrained age estimates on a series of recessional moraines in the area to ~11,800–13,900 yBP (Lepper et al., 2007). We therefore consider an average age of  $13,000 \pm 1,000$  yBP as the age of deposition of the glacial till associated with the study site.

Upland soils in the study area are dominated by Mollisols and Inceptisols (Soil Survey Staff, Natural Resources Conservation Service, United States Department of Agriculture, 2014), Chernozems and Cambisols in the WRB system (IUSS Working Group WRB, 2015). There is strong evidence that soils currently mapped as Inceptisols in the study area are in fact eroded Mollisols (Jelinski & Yoo, 2016) and have been recognized as such in both Pope County, Minnesota, and surrounding counties (Soil Survey Staff, Natural Resources Conservation Service, United States Department of Agriculture, 2017). Mollisols are particularly susceptible to classification change under high erosion rates, because the major diagnostic feature utilized for classification is the mollic epipedon (Veenstra & Burras, 2012). In the absence of other subsurface diagnostic features such as an argillic horizon, these soils become Inceptisols or Entisols if the thickness of the mollic epipedon is reduced through erosion until it no longer meets mollic criteria (Soil Survey Staff, Natural Resources Conservation Service, United States Department of Agriculture, 2014).

Upland soils in the study area are typically characterized by subsurface calcic horizons (diagnostic horizons with  $>15\%$   $\text{CaCO}_3$  equivalent by mass; Soil Survey Staff, Natural Resources Conservation Service, United States Department of Agriculture, 2014) that can have complex mechanisms of formation dependent on parent material, climate, hydrology, topography, and vegetation (Gocke et al., 2010; Mikhailova & Post, 2006). However, given the relatively young glacial sediments and landscape position of these soils, it is most likely that in our study area these calcic horizons formed *per descensum* (Mikhailova & Post, 2006), through the dissolution and leaching of carbonates from the upper portions of soil profiles and their reprecipitation deeper in the soil profile under increasing partial pressure of  $\text{CO}_2$  (Gocke et al., 2010).

### 2.1.2. Climate, Pre-European Settlement Ecology, and Land Use History

The long-term climate record from the University of Minnesota-Morris West Central Research and Outreach Center (16.5 km from our study site) has a 30-year (1981–2010 CE) annual average precipitation of 672 mm and a mean annual air temperature of 5.8 °C (Western Regional Climate Center, 2017). Annual evapotranspiration estimates for the area vary from 410–500 mm/year (Sanford & Selznick, 2013) to 533–609 mm/year

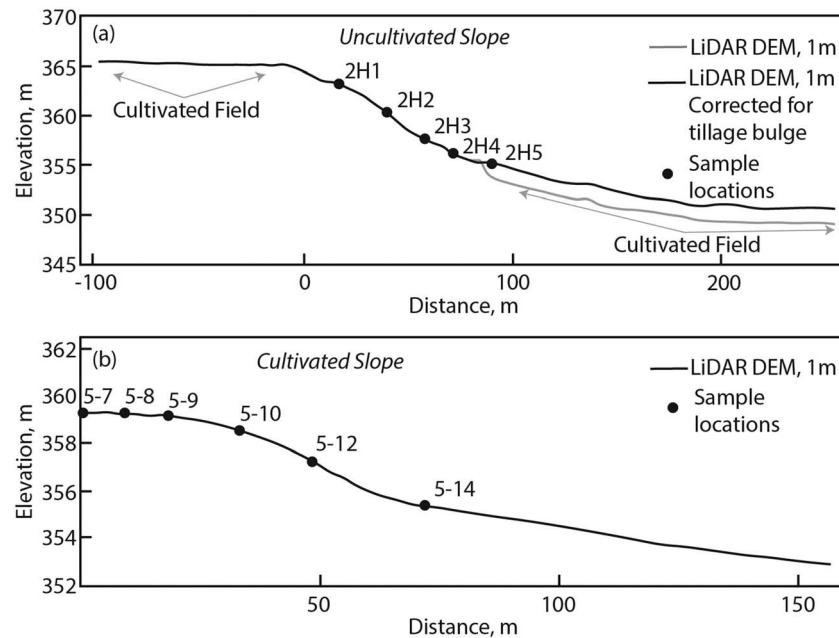


**Figure 2.** Topographical profiles of (a) uncultivated hillslope and sampling locations from light detection and ranging-derived DEM (1 m<sup>2</sup>/pixel). Distance values on the x axis are negative to correspond with scaled portions of the uncultivated hillslope in subsequent figures, where the location at 0 m is displayed at the origin. The grey line shows the raw data, which includes evidence of an edge of field tillage bulge at location 2H5. The black line details the smoothing correction made for the purposes of the Be2D simulations. (b) cultivated hillslope and sampling locations from light detection and ranging-derived DEM (1 m<sup>2</sup>/pixel).

(Baker et al., 1979). The pre-European settlement vegetation of the area was a matrix of dry, mesic, and wet grasslands (Minnesota Department of Natural Resources Staff, 1988). Both natural and anthropogenic fire disturbance was significant in this system, with typical pre-European settlement fire return intervals of less than 5 years (Frost, 2000). Additionally, burrowing mammals are common components of grassland ecosystems in Minnesota, the most widespread being the plains pocket gopher (*Geomys bursarius*), 13-lined ground squirrel (*Spermophilus tridecemlineatus*), and American badger (*Taxidea taxus*; Tester, 1995).

The paired hillslopes are separated by the Chippewa River (Figure 1); with an uncultivated (southern) hillslope under perennial grass cover, and a cultivated (northern) hillslope under annual wheat production, both on Goose Lake till, forming rolling uplands above the floodplain (Figure 1a; Harris, 2003). The uncultivated hillslope is characterized by significantly steeper slopes ( $10.3 \pm 3.0^\circ$ , slope tangents of  $0.18 \pm 0.05$ ) than the cultivated field ( $1.9 \pm 1.3^\circ$ , slope tangents of  $0.03 \pm 0.02$ ; Figures 1b and 1c). What would be considered the uppermost summit position of the uncultivated hillslope is currently located in a cultivated field (Figures 1 and 2); and thus is excluded from this study, but the hillslope does have an intermediate summit/shoulder, which has been previously identified as the most stable position on the uncultivated hillslope (De Alba et al., 2004). While agricultural activities taking place both above and below the uncultivated slope may have had the potential to impact soil properties at the sampling points on the slope itself, the soil morphology and soil properties across the uncultivated slope (with the exception of location 2H5, discussed below) do not appear to show any extensive indications of disturbance. Across the hillslope, soil organic carbon is high in the topsoil, the soil structure appeared to be granular and not mechanically modified, and there were no major morphological indications or particle size anomalies.

Documentary evidence of the lack of cultivation on the uncultivated hillslope includes the earliest archived aerial photos taken in 1939 CE (University of Minnesota, John R. Borchert Map Library, 2017) and land-owner generational memory stretching back at least into the early 1920s CE. Additionally, the uncultivated hillslope transect is recognized as a dry prairie native plant community of statewide importance (Minnesota County Biological Survey, 2003), which suggests that post-European settlement land use intensity on this hillslope has been minimal. Although these lines of evidence indicate that grazing has not been a

common practice for the 70 years prior to sampling on this site, we cannot categorically exclude the possibility of grazing activities or other anthropogenic activities prior to the early 1920s CE.

Hillslope topographical profiles were derived from a light detection and ranging digital elevation model with a resolution of 1 m<sup>2</sup>/pixel (Figure 2) and, for modeling purposes, were interpolated to a resolution of 9 m<sup>2</sup>/pixel using a median filter to remove the small-scale topographic variability. After careful investigations of the light detection and ranging data and field observations, an elevation bulge at the foot of the uncultivated hillslope was identified (Figure 2). We ascribe this to historical tillage operations, taking place on the flat cultivated field immediately below the uncultivated slope (Figure 1). This bulge is created by tillage implements throwing soil into the field from the field edge, thus truncating the soil, which would account for the lower than expected concentrations of some soil constituents observed at this location (Table 1). Including this *bulge* in model simulations could affect the modeled natural erosion rates. Therefore, for modeling purposes we reconstructed a presettlement hillslope profile by adding 1 m of elevation to the portion downslope of the tillage bulge, which currently lies in the cultivated field below the uncultivated hillslope (Figure 2a). Measured <sup>10</sup>Be<sub>m</sub> inventory at this location (2H5) was excluded during <sup>10</sup>Be<sub>m</sub> conversion model parameterization. Nevertheless, we chose to retain this sampling location in our presentation of the results because it provides information on the potential extent of disturbance.

The situation presented by this uncultivated study site is common throughout the U.S. Corn Belt, where uncultivated sites are rare and, if they do exist, often have remained uncultivated because they were steeper, drier, or wetter than other more easily cultivated sites (Corbett & Anderson, 2006). In the case of our paired study sites, the uncultivated hillslope is steeper and based on the morphological data (shallower depth to calcic horizons) may be drier than the cultivated hillslope. Our conversion models for <sup>10</sup>Be<sub>m</sub> (both the LODO and Be2D models, described below) allow us to take into account differences in slope gradient when producing erosion estimates (see section 2.6.1, Text S3.1, and equations ((9)), (S4), (S5), (S7), (S8), and (S9)). However, we do not explicitly account for potential differences in soil moisture between the slopes. For both models, the uncultivated hillslope is used to parameterize presettlement conditions on the cultivated slope (see sections 2.6.1 and 2.6.2, below).

Sample names used in this manuscript follow conventions from previous publications (De Alba et al., 2004; Papiernik et al., 2005), with the uncultivated hillslope termed the 2H transect (with sampling location one at the top and sampling location five at the bottom of the hillslope; Figure 2). Cultivated transect samples form a portion of a previously investigated east-west transect across a hillslope, termed transect 5. The locations chosen for <sup>10</sup>Be<sub>m</sub> analysis along the transect are on summit (5-7 and 5-8), shoulder (5-9 and 5-10), backslope (5-12), and footslope positions (5-14; Figure 2). The cultivated footslope position (5-14) is located within an upland drainageway or swale in the cultivated field that runs perpendicular to the hillslope profile (Figure 1). In 2007, at the time of sampling, the field had been under cultivation for ~110 years (Text S1) and under a conventional tillage management regime (annual moldboard plow and secondary tillage) for at least 40 years (Papiernik et al., 2005; Papiernik et al., 2007). Detailed background information regarding the estimation of time since the beginning of cultivation at this site is provided in the supporting information (Text S1) and references therein (Granger & Kelly, 2005; U.S. Department of the Interior, Bureau of Land Management, 2017). Previous research at this site has utilized the uncultivated hillslope as a reference for organic carbon, <sup>137</sup>Cs, and the expected distribution of inorganic carbon across the landscape with topography (De Alba et al., 2004; Papiernik et al., 2007).

## 2.2. Soil Sampling and Characterization

In June, 2007, samples were taken with a hydraulic corer as part of a larger gridded sampling scheme across the 2.7-ha cultivated field. Core morphology was described in the field, and cores were subsequently segmented, air-dried, hand-pulverized, and homogenized by depth increments sharing similar morphology. Morphological distinctions utilized to define genetic horizons included soil color, soil structure, soil texture, visible secondary carbonates, and visual differences in volume estimates of coarse fragments (Schoeneberger et al., 2011). Soil samples were air dried, hand pulverized, and sieved to separate the fine earth (<2 mm) from coarse fragments (>2 mm). The fine earth fraction (<2 mm) was utilized for characterization of soil pH, soil organic carbon (SOC), soil inorganic carbon (SIC, expressed as CaCO<sub>3</sub> equivalent), particle size distribution,

**Table 1** Meteoric  $^{10}\text{Be}$ , SOC, SIC Concentrations, and  $^{137}\text{Cs}$  Distributions

Sample location	Depth increment (cm)	Bulk density ( $\text{g cm}^{-3}$ ) < 2 mm <sup>a</sup>	Soil organic carbon ( $\text{g } 100 \text{ g}^{-1}$ ) <sup>b</sup>	Soil inorganic carbon ( $\text{g } 100 \text{ g}^{-1}$ ) <sup>b</sup>	$^{10}\text{Be}_{\text{in}}$ ( $10^7 \text{ atoms g}^{-1}$ ), Total <sup>c</sup>	$^{10}\text{Be}_{\text{m}}$ Accumulated <sup>d</sup> ( $10^7 \text{ atoms g}^{-1}$ )	$^{137}\text{Cs}$ activity (Bq/kg)
<b>Cultivated hillslope</b>							
5-7 <sup>e</sup>	0-18 <sup>f</sup>	1.27	1.4 ± 0.2	1.4 ± 0.4	12.6 ± 0.7	11.5 ± 0.8	3.4 ± 0.4
5-8	0-23	1.31	1.4 ± 0.2	0.9 ± 0.2	15.8 ± 0.3	14.7 ± 0.3	3.0 ± 0.2
5-8	23-47	1.53	0.7 ± 0.1	2.1 ± 0.6	1.18 ± 0.03	-	ND <sup>h</sup>
5-8	47-67	1.31	0.3 ± 0.1	2.2 ± 0.6	1.12 ± 0.06	-	ND
5-8	67-92	1.60	0.2 ± 0.1	2.2 ± 0.6	1.08 ± 0.04 <sup>g</sup>	-	ND
5-8	92-145	1.33	0.1 ± 0.1	2.2 ± 0.6	1.09 ± 0.02*	-	ND
5-9	0-19	1.50	1.0 ± 0.2	2.5 ± 0.7	5.18 ± 0.08	4.11 ± 0.09	2.8 ± 0.3
5-9	19-48	1.40	0.4 ± 0.1	3.0 ± 0.8	0.82 ± 0.02	-	ND
5-9	48-92	1.43	0.3 ± 0.1	2.7 ± 0.7	0.84 ± 0.03*	-	ND
5-9	92-130	1.40	0.2 ± 0.1	2.2 ± 0.6	0.82 ± 0.02*	-	ND
5-10	0-21	1.38	1.0 ± 0.2	2.2 ± 0.6	4.16 ± 0.08	3.08 ± 0.09	2.4 ± 0.2
5-10	21-75	1.19	0.2 ± 0.1	2.2 ± 0.6	1.20 ± 0.03	-	ND
5-10	75-115	1.48	0.2 ± 0.1	2.4 ± 0.7	1.12 ± 0.04*	-	ND
5-10	115-147	1.47	0.3 ± 0.1	2.4 ± 0.7	1.09 ± 0.03*	-	ND
5-12	0-18	1.22	1.2 ± 0.2	2.4 ± 0.7	3.16 ± 0.06	2.09 ± 0.08	1.3 ± 0.2
5-12	18-60	0.68	0.6 ± 0.1	4.7 ± 1.3	1.48 ± 0.04	-	ND
5-12	60-100	1.09	0.8 ± 0.1	3.8 ± 1.0	1.31 ± 0.06*	-	ND
5-12	100-130	1.29	0.6 ± 0.1	2.8 ± 0.8	0.873 ± 0.04*	-	ND
5-14	0-22	1.48	1.4 ± 0.2	0.5 ± 0.1	19.2 ± 0.3	18.1 ± 0.3	3.9 ± 0.3
5-14	22-55	1.38	1.2 ± 0.2	0.1 ± 0.1	24.8 ± 0.3	23.8 ± 0.4	1.3 ± 0.2
5-14	55-82	1.35	0.5 ± 0.1	ND	12.0 ± 0.2	10.9 ± 0.2	ND
5-14	82-122	1.34	0.2 ± 0.1	ND	1.26 ± 0.03	-	ND
5-14	122-146	1.37	0.1 ± 0.1	0.9 ± 0.2	0.782 ± 0.02*	-	ND
<b>Uncultivated hillslope</b>							
2H1	0-16	1.00	5.0 ± 0.8	1.0 ± 0.3	12.4 ± 0.4	11.3 ± 0.4	12.5 ± 0.4
2H1	16-24	1.51	2.3 ± 0.3	2.5 ± 0.7	5.20 ± 0.04	4.12 ± 0.1	3.1 ± 0.3
2H1	24-48	1.47	1.2 ± 0.2	3.0 ± 0.8	1.49 ± 0.04	-	ND
2H1	48-84	1.35	0.5 ± 0.1	2.7 ± 0.7	1.30 ± 0.05	-	ND
2H1	84-135	1.39	0.3 ± 0.1	2.3 ± 0.6	1.09 ± 0.04*	-	ND
2H2	0-16	1.09	3.9 ± 0.6	0.3 ± 0.1	11.0 ± 0.1	9.98 ± 0.1	8.4 ± 0.3
2H2	16-32	1.30	2.4 ± 0.3	2.3 ± 0.6	3.38 ± 0.07	2.31 ± 0.08	5.4 ± 0.7
2H2	32-60	1.15	1.0 ± 0.2	3.4 ± 0.9	1.09 ± 0.03	-	ND
2H2	60-87	1.51	0.4 ± 0.1	2.5 ± 0.7	0.986 ± 0.05	-	ND
2H2	87-131	1.41	0.4 ± 0.1	2.1 ± 0.6	0.947 ± 0.04*	-	ND
2H3	0-22	0.91	4.4 ± 0.7	ND	23.1 ± 0.5	18.1 ± 0.5	9.4 ± 0.4
2H3	22-40	1.10	1.5 ± 0.2	ND	21.6 ± 0.6	20.5 ± 0.6	0.8 ± 0.2
2H3	40-70	1.24	0.7 ± 0.1	ND	13.6 ± 0.2	12.6 ± 0.2	ND
2H3	70-122	1.11	0.3 ± 0.1	0.2 ± 0.1	1.97 ± 0.06*	-	ND
2H4	0-24	1.00	3.9 ± 0.6	ND	22.1 ± 0.2	21.0 ± 0.2	9.7 ± 0.6
2H4	24-58	1.19	1.2 ± 0.2	ND	16.7 ± 0.2	15.6 ± 0.2	0.2 ± 0.1
2H4	58-86	1.53	0.8 ± 0.1	ND	19.0 ± 0.3	17.9 ± 0.3	ND
2H4	86-107	1.30	0.7 ± 0.1	ND	23.1 ± 0.3	22.0 ± 0.3	ND
2H4	107-144	1.34	0.3 ± 0.1	ND	8.74 ± 0.1	7.66 ± 0.1	ND
2H5	0-23	1.16	4.0 ± 0.6	ND	26.8 ± 0.3	25.8 ± 0.3	5.9 ± 0.2
2H5	23-47	1.36	1.2 ± 0.2	ND	17.0 ± 0.6	16.0 ± 0.2	ND
2H5	47-67	1.38	0.4 ± 0.1	0.5 ± 0.1	3.53 ± 0.08	2.46 ± 0.09	ND

**Table 1** (continued)

Sample location	Depth increment (cm)	Bulk density (g cm <sup>-3</sup> ) < 2 mm <sup>a</sup>	Soil organic carbon (g 100 g <sup>-1</sup> ) <sup>b</sup>	Soil inorganic carbon (g 100 g <sup>-1</sup> ) <sup>b</sup>	<sup>10</sup> Be <sub>m</sub> (10 <sup>7</sup> atoms g <sup>-1</sup> ), Total <sup>c</sup>	<sup>10</sup> Be <sub>m</sub> (10 <sup>7</sup> atoms g <sup>-1</sup> ) Accumulated <sup>d</sup>	<sup>137</sup> Cs activity (Bq/kg)
2H5	67–98	1.25	0.4 ± 0.1	2.0 ± 0.5	1.18 ± 0.08	-	ND
2H5	98–125	1.31	0.5 ± 0.1	2.2 ± 0.6	0.881 ± 0.03	-	ND
2H5	125–150	1.63	0.1 ± 0.1	2.2 ± 0.6	0.866 ± 0.03*	-	ND

Note. SIC, soil inorganic carbon; SOC, soil organic carbon. <sup>a</sup>Soil bulk density values reported here are coarse fragment free, including only the mass of particles <2 mm in diameter. <sup>b</sup>Uncertainty reported represents the analytical uncertainty (1σ) evaluated from replicated samples. <sup>c</sup>Total <sup>10</sup>Be<sub>m</sub> concentration (<sup>10</sup>Be<sub>m,r-07KNSTD standard used for normalization (<sup>10</sup>Be/<sup>9</sup>Be ratio of 2.85 × 10<sup>-12</sup>), uncertainty reported represents the analytical uncertainty (1σ) from the mean accelerator mass spectrometry measurement. <sup>d</sup>Accumulated <sup>10</sup>Be<sub>m</sub> concentration (<sup>10</sup>Be<sub>m,λ</sub>) = <sup>10</sup>Be<sub>m,r-07</sub> - <sup>10</sup>Be<sub>m,ave</sub> = average inherited <sup>10</sup>Be<sub>m</sub>; 1.07 ± 0.31 × 10<sup>-7</sup> atoms/g. <sup>e</sup>Due to sampling limitations, 5–7 is characterized solely by the surficial (plow layer) increment, which, based on all other observations across the cultivated site is assumed to contain all profile accumulated <sup>10</sup>Be<sub>m,λ</sub>. <sup>f</sup>Sampling depth increments based on genetic soil horizon designations from Schoeneberger et al. (2011). <sup>g</sup>Measurements with an asterisk (\*) meet the criteria for inclusion in calculation of average parent material values and <sup>h</sup>ND, constituent not detected or below limit of detection for analytical method.</sub>

specific surface area (SSA), <sup>137</sup>Cs activities, and <sup>10</sup>Be<sub>m</sub> concentrations (Tables 1 and S1). Particles (typically fine gravels) that were too large in diameter to pass the 2-mm sieve (>2 mm) were retained, shaken overnight in dilute sodium hexametaphosphate to remove any adhering soil particles, oven-dried for 24 hr at 105 °C, and weighed. Coarse fragments present in the samples were typically fine gravels and accounted for, on average, 13.5 ± 0.9% of the bulk mass of the sample from the field. On the same day that physical and chemical characterization of fine earth (<2 mm) was initiated, a subsample of the air-dried material was placed in a drying oven for 24 hr at 105 °C and weighed prior to and after drying in order to account for the moisture content of the air-dried sample used for analysis. Thus, the bulk densities reported, and all other proportions of soil constituents reported in the data represent percentages of oven-dried fine-earth (<2 mm) material.

Soil pH was determined in a slurry of 5 g of air dried soil and 10 ml of 0.01 M CaCl<sub>2</sub>. Total carbon and nitrogen (g/kg) were determined by dry combustion at 800 °C using a LECO 2000 CN analyzer. SIC was determined using a pressure calcimeter, calibrated with known amounts of pure CaCO<sub>3</sub>, and reported as CaCO<sub>3</sub> equivalent (g 100/g). CaCO<sub>3</sub> equivalents were converted to SIC concentrations and subtracted from total carbon concentrations to arrive at SOC concentrations (g 100/g). <sup>137</sup>Cs activities were detected from 2007 to 2008 at 662 keV using broad energy germanium gamma spectrometers (Canberra BE3830, Landscape Dynamics Laboratory, Univ. of Manitoba, Winnipeg, Canada) with counting times ranging from 4 to 12 hr and typical detection errors of less than 10% (Li et al., 2007; Li et al., 2008). Particle size distributions were determined by laser diffraction with a silt-clay size class cutoff of 8 μm for comparison with particle size classes by sedimentation (Konert & Vandenberghe, 1997) on samples shaken and dispersed in sodium hexametaphosphate for 12 hr and run in duplicate on a laser particle size analyzer (Horiba LA960). We measured specific mineral surface area (SSA) for the <2 mm fraction of our samples after heating at 350 °C for 12 hr to remove organic matter using a TriStar 3020 Surface Area and Porosity Analyzer applying Brunauer-Emmett-Teller (BET) theory (Brunauer et al., 1938; Mayer & Xing, 2001; Wagai et al., 2009). The BET-N<sub>2</sub> method does not capture interlayer surface areas of expandable clays (Wagai et al., 2009), and therefore, our SSA determined by the BET-N<sub>2</sub> method should be considered to represent the external surface of solids present in soil samples.

Soil bulk density was determined at the same sampling locations on a set of duplicate cores by dividing the mass of fine earth (<2 mm—excluding the mass of coarse fragments >2 mm as described above) by using the sample mass after oven-drying at 105 °C for 24 hr. We thus report the bulk density of each increment as the coarse-fragment free bulk density (i.e., the density of the sampling increment including only the oven-dry mass of fine-earth [<2 mm] particles) in that increment.

### 2.3. Meteoric <sup>10</sup>Be (<sup>10</sup>Be<sub>m</sub>) Extraction and Measurement

Meteoric <sup>10</sup>Be adsorbed to mineral grains and bound to organic materials was removed through a series of acidification steps and ion exchange chromatography prior to being oxidized and analyzed by accelerator mass spectrometry (AMS). The methodology used here is modified from Ebert et al. (2012). <sup>10</sup>Be<sub>m</sub> was extracted from 0.50 g of air-dried, homogenized, and sieved (<2 mm) soil in Teflon vessels using 0.5 M HCl and 250 μg of spiked <sup>9</sup>Be carrier at 110 °C for 3 hr, after which time the sediment was removed via centrifugation and pipetting. Four millimeter of HF was added to the cation solution in two steps to bind excess Ca and Mg. After each of two HF addition steps, 10 ml of ultrapure water was added. The ultrapure water containing Be and other cations was removed from the fluoride cake via centrifugation and pipetting. Ion exchange chromatography (both anion and cation removal steps) was used to purify Be cations from the

bulk cation solution (leaching method from Ebert et al., 2012). Be-hydroxides were precipitated from the purified cation solution by titration to pH 9 through the addition of ammonia. The supernatant was decanted, and the precipitate was washed several times with ultrapure water and dried overnight at 100 °C in low-boron quartz vials. The dry precipitate was flame-oxidized at >850 °C to form BeO powder and pressed into cathodes with niobium powder for AMS analysis at PRIME Lab, Purdue University, USA. A process blank was run with each batch of nine samples.

Total  $^{10}\text{Be}_m$  concentrations ( $^{10}\text{Be}_{m,T}$  atoms/g) were calculated using measured  $^{10}\text{Be}/^9\text{Be}$  ratios from AMS (Table 1):

$$^{10}\text{Be}_{m,T}(\text{atoms/g}) = \frac{{}^9\text{Be}_{\text{carrier}}(\text{g}) \left( \frac{{}^{10}\text{Be}}{9\text{Be}}(\text{sample}) - \frac{{}^{10}\text{Be}}{9\text{Be}}(\text{blank}_{\text{ave}}) \right) N_A}{M_{10\text{Be}} g_{\text{sample}}}, \quad (1)$$

where  ${}^9\text{Be}_{\text{carrier}}(\text{g})$  is the total amount of Be carrier added to the sample,  $^{10}\text{Be}/^9\text{Be}(\text{sample})$  and  $^{10}\text{Be}/^9\text{Be}(\text{blank}_{\text{ave}})$  are the  $^{10}\text{Be}/^9\text{Be}$  ratios of the sample and of all blanks (averaged),  $N_A$  is Avogadro's number,  $M_{10\text{Be}}$  is the molar mass of  $^{10}\text{Be}$  (g/mol), and  $g_{\text{sample}}$  is the amount of soil sample added (g).

#### 2.4. Calculation of $^{10}\text{Be}$ Inventories

Measurements of *total* meteoric  $^{10}\text{Be}$  concentrations ( $^{10}\text{Be}_{m,T}$  atoms/g) include the *inherited*  $^{10}\text{Be}_m$  present in the glacial till when it was deposited ( $^{10}\text{Be}_{m,I}$  atoms/g) and the  $^{10}\text{Be}_m$  *accumulated* during the period of soil formation since the land surface was ice free ( $^{10}\text{Be}_{m,A}$  atoms/g). When  $^{10}\text{Be}_{m,T}$ ,  $^{10}\text{Be}_{m,I}$ , or  $^{10}\text{Be}_{m,A}$  are discussed, they are explicitly identified in the text with the corresponding subscripts.

The average concentration of  $^{10}\text{Be}_{m,I}$  from the glacial till parent material at our study area was estimated as follows: The average  $^{10}\text{Be}_{m,T}$  concentration from the bottom depth increment of all sampling locations, as well as any other sampling increments that were below the calcic horizon and determined to be relatively unaltered (i.e., C horizons), were included in the average. The bottom sampled depth increment at each location was determined from the soil morphology. In particular, we determined the location of the calcic horizon (a horizon showing strong accumulation of calcium carbonate) in each of the upper slope sampling locations by a combination of morphological indicators in the field, including color and reaction to weak hydrochloric acid (Table S1). In this case we ensured that at least one additional genetic horizon was sampled below the bottom depth of the calcic horizon. In lower slope positions without a calcic horizon, the bottom depth increment was sampled as nearly as possible to a depth of 150 cm (Table S1).

For each measured depth increment ( $i$ ), the inventory of  $^{10}\text{Be}_{m,A}$  is the excess of  $^{10}\text{Be}_{m,T}$  over  $^{10}\text{Be}_{m,I}$ , where  $^{10}\text{Be}_{m,I,\text{ave}}$  is the average inherited  $^{10}\text{Be}_m$  concentration across all samples:

$$^{10}\text{Be}_{m,A,i} = ^{10}\text{Be}_{m,T,i} - ^{10}\text{Be}_{m,I,\text{ave}}, \quad (2)$$

and if, by equation (2),  $^{10}\text{Be}_{m,A,i} < 0$ , then  $^{10}\text{Be}_{m,T,i}$  is assumed to be equal to  $^{10}\text{Be}_{m,I,i}$ , and  $^{10}\text{Be}_{m,A,i}$  is set to 0.

The total accumulated, noninherited  $^{10}\text{Be}$  inventory ( $I_A$  [atoms/L<sup>2</sup>]) for each sampling location is then

$$I_A = \sum_{i=1}^n ^{10}\text{Be}_{m,A,i} \rho_b \left( (h - z_{b,i}) - (h - z_{t,i}) \right), \quad (3)$$

where  $^{10}\text{Be}_{m,A,i}$  is the concentration of accumulated  $^{10}\text{Be}_m$  [atoms/M] in increment  $i$ ;  $\rho_b$  is the increment dry bulk density [M/L<sup>3</sup>],  $h$  is the elevation of the soil surface, and  $z_{b,i}$  and  $z_{t,i}$  are the bottom and top elevation of the sampled increment, respectively,  $i = 1$  is the top (surficial) depth increment; and  $i = n$  is the bottom depth increment. Thus in (3), and all equations that follow, we define  $z$  [L] as the absolute elevation (above sea level),  $h$  [L] as the elevation of the soil surface, and  $d = h - z$  [L] as depth below the soil surface. Inventories of  $^{10}\text{Be}_{m,T}$ ,  $^{10}\text{Be}_{m,I}$ ,  $^{10}\text{Be}_{m,A}$ , SOC, inorganic carbon (converted from CaCO<sub>3</sub> equivalent), and  $^{137}\text{Cs}$  were calculated to 1.5 m (depth of deepest observation in data set) for all sampling locations by extending observed values of the lowest depth increment to 1.5 m if it did not extend that far (Table S2). We chose 1.5 m as the lowest depth of inventory calculation because it was our lowest sampling depth based on morphological criteria described above. With the exception of sampling locations 2H3 and 2H4,  $^{10}\text{Be}_m$  concentrations in the lowest depth increment had declined to within the range of estimated inheritance for Des Moines lobe glacial till from this and other studies (Balco, 2004; Belmont et al., 2011). This resulted in a

maximum of 28 cm of gap-filling for sampling location 2H3, but in all cases the contribution of the gap-filled portion was <5% of the inventory. All inventories for other soil constituents discussed in this study were calculated as in equation (3), above (Table S2).

### 2.5. $^{137}\text{Cs}$ Conversion Models for Estimating 53-Year Average Erosion Rates

Procedures for deriving erosion rate estimates from the variability of radionuclide inventories across a hillslope or landscape are typically called conversion models, for their role in converting observations of radionuclide inventories to quantitative rates of erosion or deposition (Walling et al., 2002). Every such conversion model necessarily requires a set of assumptions, many of which, depending on the system, may be strictly false and can complicate the interpretation and meaningfulness of the output rates (Parsons & Foster, 2011).

For  $^{137}\text{Cs}$ , these assumptions include (1) uniform deposition of  $^{137}\text{Cs}$  across the landscape, which is assumed to be accurately reflected in the chosen reference inventory for the study site, but has been shown to be violated even under natural conditions (Kaste et al., 2006; Parsons & Foster, 2011); (2) wet deposition as the dominant source of fallout (Basher et al., 1995); (3) strong and rapid affinity of Cs to fine soil particles, which may in fact be a more variable and longer process than often assumed (Bunzl et al., 1995); (4) for cultivated systems, a homogenous distribution of  $^{137}\text{Cs}$  throughout the plow layer; and (5) redistribution across the landscape solely due to the movement of  $^{137}\text{Cs}$  across the soil surface, which has been shown to be violated in agricultural landscapes under artificial drainage (Chapman, 2001). We note that there is no artificial drainage installed at our study site, but nonetheless, these observations suggest that assumptions of identical down-profile advection and diffusion across the landscape may not be valid. The net implications of violations of these assumptions mean that true uncertainties in  $^{137}\text{Cs}$ -derived erosion rates are much larger than typically reported (Parsons & Foster, 2011).

Despite these limitations,  $^{137}\text{Cs}$  conversion models continue to be widely used (i.e., Abrahams et al., 2018; Tuo et al., 2018), and studies have shown that  $^{137}\text{Cs}$  conversion models can reasonably reproduce the pattern and magnitude of erosion rates produced by process-based models and direct observations (Porto et al., 2003), provided conversion model selection is undertaken with care (Li et al., 2010), and uncertainties are properly evaluated to allow reasonable interpretation of the resulting rates (Zhang et al., 2015). For these reasons, despite the limitations inherent in point-estimates of soil redistribution derived from  $^{137}\text{Cs}$ , we choose to utilize  $^{137}\text{Cs}$  inventories observed at our study site to derive erosion rate estimates to lend comparative context to our  $^{10}\text{Be}_m$  model results. This approach is reasonable because our major objective was to compare the results of presettlement and postsettlement erosion rate estimates at our study site, which often differ by orders of magnitude. Thus, the results from our  $^{137}\text{Cs}$  observations and conversion models provide further context for our postsettlement  $^{10}\text{Be}_m$  results and add to the body of evidence for understanding differences in presettlement and postsettlement erosion rates.

A foundational set of conversion models for  $^{137}\text{Cs}$  have been developed into open source tools (Walling et al., 2002; Walling & He, 2001). A subset of four of these conversion models designed for use in cultivated systems includes a proportional model (PM) and three mass balance models (MBM1, MBM2, and MBM3, respectively), which successively increase in complexity of parameterization and input data required (Walling et al., 2002). Previous work has shown the PM to be least adequate for deriving quantitative erosion and deposition rates, and the accuracy of each of the MBMs to be dependent on the actual pattern and type of erosion across a hillslope or landscape (Li et al., 2010).

Within this set of  $^{137}\text{Cs}$  conversion models, we chose to utilize MBM2 and MBM3 (Table 2), which are generally considered to be more accurate models than the PM and MBM1, but require additional input parameters (Hassouni & Bouhlassa, 2006; Walling & He, 2001). Unlike the PM and MBM1, MBM2, and MBM3, each take into account the variability in  $^{137}\text{Cs}$  fallout over time, starting in 1954. In each case, we utilized the northern hemisphere annual deposition estimates included in a data file with the model packages (Walling & He, 2001). In addition to the time-variant fallout flux of  $^{137}\text{Cs}$ , MBM2 requires the following additional parameters: (1) a particle size correction factor,  $\psi$ , for eroding sediment, and  $\psi'$  for deposited sediment; (2) the proportion of annual  $^{137}\text{Cs}$  input susceptible to removal by erosion ( $\gamma_{\text{MBM}}$ ); (3) the relaxation mass depth ( $H_{\text{MBM}}$ ); (4) the mass plow depth ( $d_m$ , mass of soil contained in the plow layer, a product of bulk density and tillage depth); and (5) the year of tillage commencement, which we set as the same

**Table 2**  
*Basic Characteristics of the Erosion Models Used in This Study*

Model	Structure	Input	Output
LODO – Loss Only-Diffusion Only	Simplified one-dimensional simulation of $^{10}\text{Be}_m$ concentration profiles over time. Points are independent of each other. Only vertical diffusion and net soil flux from the point are considered. Includes both presettlement (natural) and postsettlement (agricultural) modules.	$^{10}\text{Be}_m$ concentration depth profiles + additional parameters	Presettlement and postsettlement erosion rate estimates
Be2D	Spatially explicit two-dimensional model simulating the behavior of $^{10}\text{Be}_m$ on a hillslope. The model concurrently simulates (1) vertical processes redistributing $^{10}\text{Be}_m$ at the profile scale and (2) processes redistributing $^{10}\text{Be}_m$ longitudinally across the hillslope. Includes both presettlement (natural) and postsettlement (agricultural) modules.	$^{10}\text{Be}_m$ concentration depth profiles, $^{10}\text{Be}_m$ inventories, topography + additional parameters	Presettlement and postsettlement erosion rate estimates
MBM2	Mass balance model solved numerically which considers the time-variant fallout of $^{137}\text{Cs}$ and the fate of the freshly deposited fallout prior to soil incorporation. Appropriate for application in agricultural settings only. Soil accumulation points are affected by soil loss points. Does not take into account tillage erosion.	$^{137}\text{Cs}$ inventories, $^{137}\text{Cs}$ fallout rates over time + additional parameters	53-year-average erosion rate under agricultural management
MBM3	Mass balance model solved numerically which considers the time-variant fallout of $^{137}\text{Cs}$ and the fate of the freshly deposited fallout prior to soil incorporation. Appropriate for application in agricultural settings only. Soil accumulation points are affected by soil loss points. Takes into account soil redistribution by tillage.	$^{137}\text{Cs}$ inventories, $^{137}\text{Cs}$ fallout rates over time, tillage constant + additional parameters	53-year-average erosion rate under agricultural management
WaTEM	Process-based Water and Tillage Erosion Model (van Oost et al., 2000). Estimates tillage erosion using a diffusion equation and water erosion using a modified version of the Revised Universal Soil Loss Equation (RUSLE).	Topographic, environmental, and management parameters	Erosion rates under agricultural management

year as the initiation of  $^{137}\text{Cs}$  fallout, 1954 CE (Walling et al., 2002). MBM3 utilizes the same parameters as MBM2 but includes an additional tillage erosion module, which requires the use of a tillage constant ( $\phi$ ) that was estimated based on typical parameter ranges (Walling et al., 2002) and previous modeling work at the study site (Li et al., 2010).

Previous work has shown that the parameters that most strongly impact estimated erosion rates are the  $^{137}\text{Cs}$  reference value ( $^{137}\text{Cs}_{\text{ref}}$ ), followed by the particle size correction factors ( $\psi$  and  $\psi'$ ), and the tillage depth ( $d_{\text{till}}$ ; Li et al., 2010; Zhang et al., 2015). Therefore, we either directly calculated these values from additional data available to us at our study site (in the case of  $\psi$  and  $\psi'$ ) or conducted multiple model runs over a reasonable potential range of parameter values (for  $^{137}\text{Cs}_{\text{ref}}$  and  $d_m$ ; Table S3). We utilized a range of three independently derived reference inventories ( $^{137}\text{Cs}_{\text{ref}}$ ) in the model runs, all based on previous data collected at the study site: 2,224 Bq/m<sup>2</sup> (Li et al., 2008; from a single core in an adjacent native undisturbed wet grassland); 2,093 Bq/m<sup>2</sup> (Li et al., 2007; the average of seven cores taken in a native grassland near the study site); and 1,893 Bq/m<sup>2</sup> (an additional decay-corrected reference value derived from the Li et al., 2008, study). Each of these  $^{137}\text{Cs}_{\text{ref}}$  values was utilized as a reference for previous work at the study site. The average of  $^{137}\text{Cs}$  inventories across the uncultivated hillslope in this study (none of which are appropriate in isolation to utilize as  $^{137}\text{Cs}_{\text{ref}}$  values because none are located on stable landscape positions) is 2,186 Bq/m<sup>2</sup>, and thus by using the three previous values mentioned we have spanned a reasonable range of possible  $^{137}\text{Cs}_{\text{ref}}$  values at our study site. Other parameters in the models have been shown to have a smaller impact on the resulting rates, and in these cases we chose to utilize values from previous studies at our site or from reasonable parameter ranges in the literature (Walling et al., 2002; Tables S3 and S4). These input parameter combinations resulted in 18 independent model runs for MBM2 and MBM3 at each sampling location (Table S3), and we report erosion rate estimates from these models as the mean and standard deviation ( $1\sigma$ ) of the 18 model runs for MBM2 and MBM3, respectively. The parameter values utilized in each of the model runs and the references relied upon to choose these parameter values are identified in Table S3.

We calculated the particle selectivity factors  $\psi$  and  $\psi'$  from the organic matter-free SSA data for topsoils at our study site (Tables S1, S3, and S4) utilizing equations from He and Walling (1996), reviewed in Walling et al. (2002):

$$\Psi = \left( \frac{SSA_{ms}}{SSA_{sl}} \right)^\nu, \quad (4)$$

where  $SSA_{ms}$  is the SSA of mobilized sediment (assumed to be the topsoil sediment at the footslope location 5-14);  $SSA_{sl}$  is the SSA of topsoil at each of the upslope sampling points, respectively; and  $\nu$  is assumed to be a constant with a value of 0.65 (Walling et al., 2002). Similarly,

$$\Psi' = \left( \frac{SSA_{ds}}{SSA_{ms}} \right)^\nu, \quad (5)$$

where  $S_{ds}$  is the SSA of deposited sediment (assumed to be the topsoil sediment at the footslope location 5-14),  $S_{ms}$  is the average SSA of topsoil for all of the upslope sampling points, and  $\nu$  is the same as that of (4).

Previous modeling work has shown that MBM2 best represents the true pattern and magnitude of erosion when water erosion is dominant, while MBM3 may be the best model choice when water and tillage erosion occur at similar magnitudes or intensities (Li et al., 2010). The latter is most likely the case at our study site (Li et al., 2007), although it is important to realize that the magnitude and intensities of tillage and water erosion vary within sites at the landscape and hillslope scale, so any one model is not likely to reflect the true magnitude of erosion when applied across all sampling points. Therefore, our use of two models allows us to represent some of the structural uncertainty in the results from  $^{137}\text{Cs}$  conversion models, rather than relying on a single model to produce erosion rate estimates.

## 2.6. $^{10}\text{Be}_m$ Conversion Models

### 2.6.1. Loss Only, Diffusion Only (LODO): Low Diffusion and High Diffusion Cases

The first conversion model we evaluate for  $^{10}\text{Be}_m$  modifies an approach taken by Johnson et al. (2014) to derive the rate and depth dependence of bioturbation using  $^{10}\text{Be}_m$ . This is a one-dimensional model that predicts the vertical profile of  $^{10}\text{Be}_m$  concentrations over time (Table 2). Our modified version can be considered a *loss only, diffusion only* (LODO) model of  $^{10}\text{Be}_m$  depth distribution with time (Table 2). In the context of other numerical modeling efforts and  $^{10}\text{Be}_m$  studies, the soils at our study site (characterized by high pH values, moderate clay contents of mixed mineralogy, and lack of morphological evidence for significant clay illuviation) would be considered high-affinity systems with respect to  $^{10}\text{Be}_m$ , enabling us to reasonably make the simplifying assumption of downward transport of  $^{10}\text{Be}_m$  by diffusion only (Boschi & Willenbring, 2016; Campforts et al., 2016; Willenbring & von Blanckenburg, 2010). However, because the LODO model considers only net erosion from a particular location on the landscape, we limit the application of these simplified models to eroding positions on upper hillslopes (summits, shoulders, and backslopes) and do not apply it to lower hillslope positions (footslopes and toeslopes). Unlike short-lived radionuclides such as  $^{137}\text{Cs}$ ,  $^{210}\text{Pb}$ , and  $^7\text{Be}$ , which would have had the majority of their current inventories deposited under modern conditions of cultivation at our study site,  $^{10}\text{Be}_{m,A}$  inventories were largely established under natural conditions and thus necessitate additional modeling steps to estimate presettlement inventories and depth distributions. The LODO model therefore consists of two parts: (1) a one-dimensional numerical model of the long-term diffusion of atmospherically deposited radionuclides into soils under conditions of natural erosion to estimate presettlement  $^{10}\text{Be}_m$  vertical distributions and inventories, followed by (2) a postsettlement routine assuming annual tillage and homogenization of the plow layer, which further evolves the presettlement profiles.

To implement the first (pre-settlement) portion of the LODO model, the soil profile is discretized, and downward mobility of  $^{10}\text{Be}_m$  from the soil surface is modeled as a diffusive process with depth dependent diffusivity:

$$\frac{\partial C_{\text{Be}}}{\partial t} = \frac{\partial}{\partial z} \left( D_s(h-z) \frac{\partial C_{\text{Be}}}{\partial z} \right), \quad (6)$$

where  $C_{\text{Be}}$  is the soil concentration of  $^{10}\text{Be}_m$  (atoms/M),  $t$  is time (year), and  $D_s(h-z)$  [ $\text{L}^2/\text{t}$ ] is the diffusion

constant at depth  $d$ , where  $d = h - z$  is the depth below the soil surface. The relationship between depth from the surface and  $D_s$  is modeled as decreasing exponentially with depth:

$$D_s(\mathbf{h}-z) = D_{s0} e^{-\frac{(h-z)}{d_e}}, \quad (7)$$

where  $D_{s0}$  is the diffusion constant at the soil surface [ $L^2/t$ ] and  $d_e$  is the  $e$ -folding depth [ $L$ ], which defines the exponential function. All deposited  $^{10}\text{Be}_m$  is assumed to enter the surficial depth increment equally prior to diffusion. A natural erosion term ( $E_{\text{nat}}$  [ $L/t$ ]) is then included whereby the profile is further discretized and the surface layer is eroded per the  $E_{\text{nat}}$  rate prior to proceeding to the next time step. This effectively advects the  $^{10}\text{Be}_m$  concentration profile upward by removing surface layers (Johnson et al., 2014; Kirkby, 1985):

$$d_{t+1} = d_t - E_{\text{nat}} t, \quad (8)$$

where  $d_{t+1} = h - z$  [ $L$ ] is the depth below the soil surface at time  $t + 1$  and  $d_t = h - z$  [ $L$ ] is the depth below the soil surface at time  $t$ . The depth increment with  $d = 0$  is subsequently set to the soil surface, and an equivalent number of additional depth increments are added from below to maintain a constant profile depth. New material entering the profile from below as a result of erosion at the surface (and thus upward advection of the concentration profile) is assumed to have a  $^{10}\text{Be}_{m,1}$  concentration of  $1.07 \times 10^7$  atoms/g, which is the average inheritance value in the glacial till parent material at the study site. This numerical model is run for the length of landscape development in 1-year time steps ( $t = 1$  year), with the total length of the model run ( $T$ ) constrained to 13,000 years (section 2.1.1), and a  $^{10}\text{Be}_m$  deposition rate ( $P_{\text{Be}}$ ) of  $1.3 \times 10^{-6}$  atoms  $\cdot$  cm $^{-2}$   $\cdot$  year $^{-1}$ . Detailed background information regarding the choice of  $^{10}\text{Be}_m$  deposition rate can be found in Text S1 and references therein (Chen et al., 2017; Field & Schmidt, 2009; Graly et al., 2011; Heikkila et al., 2008, 2013, 2014).

We then iteratively solve the model for best fit solutions for  $D_{s0}$ ,  $d_e$ , and  $E_{\text{nat}}$  that minimize model root-mean-square error relative to measured values of  $^{10}\text{Be}_m$  under each of two different presettlement scenarios that bracket the likely range of values for these variables in the LODO model at our study site (Text S2). These scenarios are described in Text S2 and are henceforth referred to as the Loss Only, Diffusion Only-Low Diffusion Scenario (LODO-Low; with best fit values of  $D_{s0} = 0.2$  cm $^2$ /year and  $d_e = 5$  cm), and Loss Only Diffusion Only-High Diffusion Scenario (LODO-High; with best fit values of  $D_{s0} = 0.5$  cm $^2$ /year and  $d_e = 28$  cm).

As  $T$ ,  $D_{s0}$ ,  $d_e$ , and  $P_{\text{Be}}$  are constrained in each of these scenarios, these parameters can then be applied in an additional model run to estimate the presettlement  $^{10}\text{Be}_m$  concentration depth profile at each eroding cultivated transect position (5-7, 5-8, 5-9, 5-10, and 5-12) with a simplified estimate of the magnitude of net soil loss ( $E_{\text{nat}}$  for this model) scaled relative to the slope of the uncultivated hillslope positions:

$$E_{\text{nat},j} = E_{\text{nat,uncult}} \frac{S_j}{S_{\text{uncult}}}, \quad (9)$$

where  $E_{\text{nat},j}$  is the natural erosion rate at location  $j$  on the cultivated slope,  $E_{\text{nat,uncult}}$  is the average uncultivated erosion rate (Text S2),  $S_j$  is the slope tangent ( $dh/dx$ , where  $x$  [ $L$ ] is the longitudinal distance across the hillslope) at location  $j$  on the cultivated slope, and  $S_{\text{uncult}}$  is the slope tangent of the uncultivated slope. This model is reasonable because even though the uncultivated site has steeper slopes than the cultivated site, all of these slopes are still well within the range where colluvial soil transport scales linearly with curvature (Roering et al., 1999), and hence with slope where only net soil loss from the point of interest is considered, and each sampling position is considered independently. To estimate the sensitivity of various parameter estimates on the presettlement profiles derived for the cultivated sampling locations (5-7, 5-8, 5-9, 5-10, 5-12), we conducted 1,000 Monte Carlo runs of the presettlement profile by randomly selecting parameter combinations from a search space within  $\pm 10\%$  of the best-estimated values (Table S4).

The postsettlement step was implemented as a separate routine, where the presettlement concentration profiles are further evolved over a 110-year postsettlement time period. Each of the 1,000 presettlement  $^{10}\text{Be}_m$  profiles (derived from the Monte Carlo simulations) at each cultivated sampling location was run through a postsettlement module assuming complete annual homogenization of the plow layer ( $d_{\text{till}}$ ) and erosion at a range of potential rates ( $E_{\text{post}}$ ) on 1-year time steps. As in the presettlement module, the erosion rate

( $E_{\text{post}}$ ) effectively advects the  $^{10}\text{Be}_m$  profile upward by removing surface increments (equation (8)). Subsequently, when time since initial cultivation and plow layer  $^{10}\text{Be}_m$  concentrations are constrained, a single solution for  $E_{\text{post}}$  is possible based on a log linear regression of the numerical modeling results for a range of erosion rates, with parametrical uncertainty evaluated by the range in outcomes from the 1,000 Monte Carlo simulations (Figure S1).

### 2.6.2. Be2D

Be2D is a coupled soil-hillslope model allowing simulation of the chemical sorption behavior of  $^{10}\text{Be}_m$  concurrently with physical redistribution processes such as soil creep, overland flow erosion, tillage, bioturbation, and clay migration (Table 2; Campforts et al., 2016). Parameter values are constrained using a two-stage strategy. In a first stage, Be2D parameters associated with natural, presettlement processes ( $E_{\text{nat}}$ ) are optimized using  $^{10}\text{Be}_m$  data measured along the uncultivated slope. In a second stage, we estimate postsettlement ( $E_{\text{post}}$ ) erosion/deposition required to simulate observed  $^{10}\text{Be}_m$  along the cultivated slope. The latter is done by simulating presettlement dynamics with the parameter values derived in the first stage and constraining postsettlement processes (tillage and rill/inter-rill erosion via overland flow) using a second optimization routine. Details of the Be2D model and parameter selection and optimization are provided in Text S3 and references therein (Campforts et al., 2016; Campforts & Govers, 2015; Govers et al., 2007; van Oost et al., 2003).

Soil fluxes and erosion rates are derived from the dynamic evolution of topography during model runs (Movies S1 and S2). The transient nature of the hillslopes at our study site, where natural postglacial landscape evolution is succeeded by a period of intense cultivation, precludes the use of a steady state topography. To overcome the lack of a known paleo-surface (the elevation at 13,000 yBP), we applied an iterative inversion method based on Višnjević et al. (2018). The inversion method allows the reconstruction of a paleo-surface for any given set of model parameter values and a measured, present day, topography. A detailed discussion of the methodology can be found in Text S3.2 and figures, tables, and references therein (Campforts & Govers, 2015, Višnjević et al., 2018; Figure S2 and Table S5). Briefly, during every model run, a unique set of parameter values is used. In a first model stage, the paleo-surface is reconstructed following the procedure outlined in Table S5. Erosional processes simulated during paleo-surface reconstruction include natural soil creep (S4), tillage erosion (S5), and overland flow erosion (S7–S10). Once the paleo-surface for a given set of parameter values is optimized, a full forward Be2D model is executed using the same set of parameter values and the derived paleo-surface as the initial topography. The paleo-surface reconstruction is thereby explicitly integrated in the model and executed for every model iteration.

Parameter values were constrained using a global genetic optimizing algorithm with 20,000 and 28,000 successive iterations to reach an optimal solution for respectively the uncultivated (stage one) and cultivated slope (stage two), respectively. We use the Nash-Sutcliffe coefficient ( $NS$ ) to calculate the goodness of fit between observed ( $O$ ) and modeled ( $M$ )  $^{10}\text{Be}_m$  concentrations and inventories:

$$NS = 1 - \frac{\sum_{i=1}^{nb} (O_i - M_i)^2}{(O_i - \bar{O})^2}, \quad (10)$$

where  $O$  is the observed value,  $M$  is the modeled value, and  $nb$  is the number of observations.  $NS$  ranges between  $-\infty$  and 1. The  $NS$  coefficient was initially developed to evaluate hydrological modeling performance (Nash & Sutcliffe, 1970). Model performance is assumed to be optimal when  $NS = 1$ , indicating that 100% of the measured data variance is represented by the model. If  $NS \leq 0$ , model performance is unacceptable with the mean of the observed data being at least as good a predictor as the modeled values. The use of  $NS$  coefficients for Be2D parameter value optimization has proven successful in a range of geophysical settings and parameter sensitivity analysis revealed satisfactory model performance for  $NS$  values  $>0.5$  (Campforts et al., 2016). Details on the model assumptions can be found in Text S3.3. Evaluated parameter ranges and model performance regarding the uncultivated and cultivated slope can be found in Text S3.4–3.5 and Text S3.6–3.7, respectively.

### 2.6.3. $^{10}\text{Be}_m$ Conversion Model Error Analysis

Three sources of uncertainty (measurement, parametrical, and structural) in our model analysis were evaluated. Measurement uncertainty due to  $^{10}\text{Be}$  AMS errors and bulk density variability was included in all

erosion rate estimates. For the LODO and Be2D models, parametrical uncertainty was evaluated through Monte Carlo simulations in which models were run 1,000 times over a range of  $\pm 10\%$  of the best-estimated input parameters (Table S4). This range encompassed reasonable values of input parameters as determined from the literature and previous studies (Text S2, Text S3, Campforts et al., 2016). Model structural uncertainty (systemic error due to model structure) was evaluated by intercomparison of results through paired  $t$  tests of result sets across the cultivated hillslope.

### 2.7. Modern Erosion Through WaTEM Estimates

Erosion by the combined effects of tillage and water was estimated using the WaTEM (Table 2, van Oost et al., 2000). Water erosion ( $\text{tons} \cdot \text{ha}^{-1} \cdot \text{year}^{-1}$ ) in the WaTEM model is based on the RUSLE (Revised Universal Soil Loss Equation) model (Renard et al., 1997),

$$A = R * K * LS * C * P, \quad (11)$$

where  $A$  is the average annual amount of soil loss ( $\text{tons} \cdot \text{ha}^{-1} \cdot \text{year}^{-1}$ ),  $R$  is the rainfall-erosivity factor ( $\text{MJ mm} \cdot \text{hr}^{-1} \cdot \text{ha}^{-1} \cdot \text{year}^{-1}$ ),  $K$  is the soil erodibility factor ( $\text{tons hr MJ/mm}$ ),  $LS$  is a topographical slope and length factor [ $L/L$ ],  $C$  is a dimensionless crop erosivity factor, and  $P$  is a dimensionless erosion control factor.

In WaTEM, tillage erosion is modeled as a diffusion process,

$$Q_{s,t} = -k_{\text{till}} S, \quad (12)$$

where the net downslope flux of soil ( $Q_{s,t}$ ) is proportional to the instantaneous local slope gradient ( $S = dh/dx$ , where  $x$  [L] is the longitudinal distance across the hillslope). We parameterized the model from previously published work at the study site, which assumed a moldboard plowing plus two disking operations annually, giving a tillage transport coefficient ( $k_{\text{till}}$ ) of  $718 \text{ kg/m}$  (Papiernik et al., 2005; Schumacher et al., 2005). To approximate the RUSLE factors, a corn/soybean/wheat rotation for the past 45 years was assumed. Model coefficients were a rainfall-runoff erosivity factor ( $R$ ) of 90, a soil erodibility factor ( $K$ ) of 0.28, a cover/management factor ( $C$ ) of 0.21, and an erosion control practice factor ( $P$ ) of 1 (Table S4).

### 2.8. Utilization of Carbonate Depth Profiles to Constrain $E_{\text{post}}$ Estimates

As a tracer independent of  $^{10}\text{Be}_m$  but relevant over the timescales of soil formation, we utilize the depth distributions of SIC (as  $\text{CaCO}_3$  equivalent) to provide additional constraints on  $E_{\text{post}}$  estimates from our LODO and Be2D models. In particular, we consider the depth to-and thickness of-carbonate-enriched subsurface calcic horizons across our cultivated hillslope. Because the calcic horizons at our study site were most likely formed *per descensum*, the depth and thickness of these horizons are highly dependent upon the partitioning of precipitation into infiltration and runoff, which, under presettlement conditions, would have been strongly linked to topography in the relatively homogeneous tills of our study area (Lin et al., 2005).

We mined the National Cooperative Soil Survey (NCSS) Soil Characterization Database (National Cooperative Soil Survey [NCSS], 2017) for laboratory characterization data of soils, which occur on upper hillslope positions in Pope County, Minnesota, and all seven surrounding counties. This database search resulted in a total of 54 unique soil profiles in 11 different soil series collected in agricultural fields between 1968 and 1993 CE. The 54 soil profiles fall into three soil Great Groups (Soil Survey Staff, Natural Resources Conservation Service, United States Department of Agriculture, 2014): Hapludolls ( $n = 29$ ), Calciudolls ( $n = 6$ ), and Eutrudepts ( $n = 19$ ). These Great Groups differ mainly in their depth to calcic horizons (Figure 3 and Text S4), in the order Hapludoll > Calciudoll > Eutrudept. Therefore, the Hapludoll profiles represent a high-end constraint on depth to carbonates in our soil profiles under presettlement conditions. The depth profiles of  $\text{CaCO}_3$  equivalent observed in the upper hillslope positions (2H1 and 2H2) of the uncultivated slope show a significantly shallower calcic horizon (identified by the peak in calcium carbonate equivalent) than those on the upper hillslope positions of the cultivated slope (Figure 3). This observation, and the distribution of great groups across slope gradients in the NCSS database (National Cooperative Soil Survey [NCSS], 2017; Figure 3), supports our use of the Hapludoll great group as the most conservative (i.e., deepest depth to calcic horizon) case for the cultivated hillslope, which is characterized by lower slope gradients than the uncultivated slope.

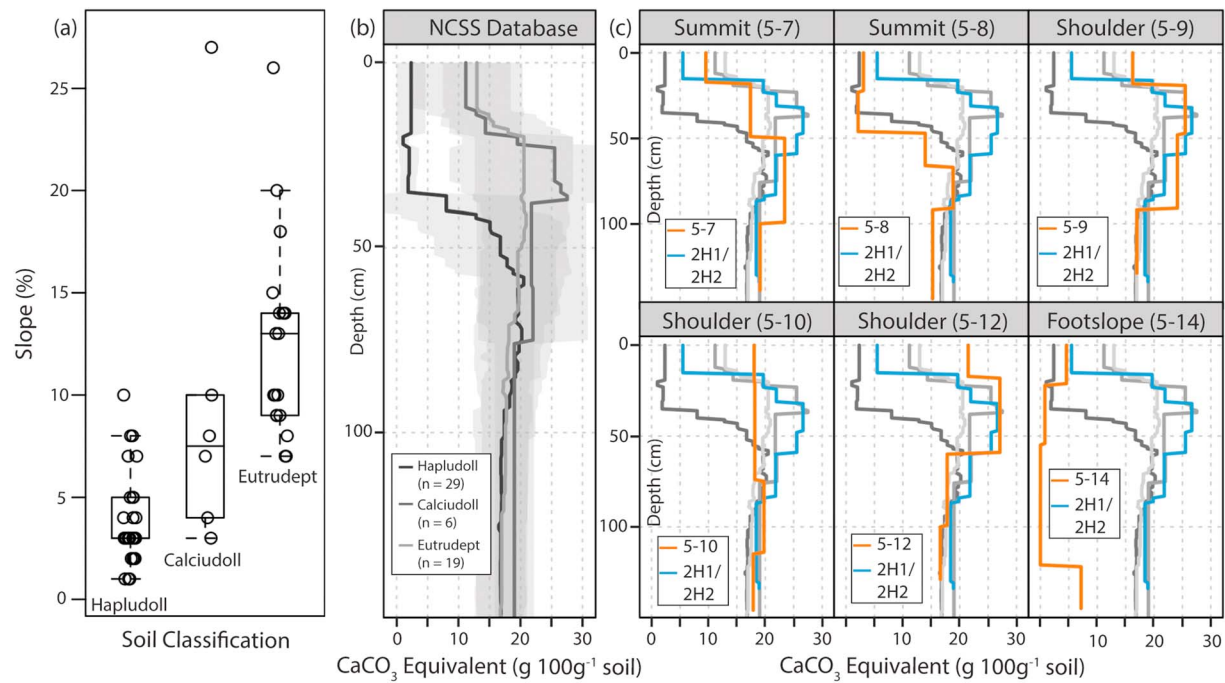


**Figure 3.** (a) Box plots of topographic slope (%) for three soil Great Groups (Soil Survey Staff, Natural Resources Conservation Service, United States Department of Agriculture, 2014) occurring at summit, shoulder, and backslope positions in Pope County, Minnesota, and all seven adjacent counties, from the National Cooperative Soil Survey (NCSS) database (National Cooperative Soil Survey [NCSS], 2017). (b) Average depth profiles of CaCO<sub>3</sub> equivalent for Hapludoll, Calciudoll, and Eutrudept profiles in the NCSS database in Minnesota (National Cooperative Soil Survey [NCSS], 2017). Note that the depth to the carbonate-enriched calcic horizon decreases from Hapludolls to Eutrudepts. The shaded grey regions represent  $\pm 1$  standard deviation from the mean, calculated from available data for each individual 1-cm depth increment using the AQP package in R (Beaudette et al., 2013). (c) Depth distributions of CaCO<sub>3</sub> equivalent at each sampling location (orange) on the cultivated hillslope plotted against upper hillslope positions (2H1 and 2H2 represented by a single, depth-averaged profile) on the uncultivated slope (blue) and average CaCO<sub>3</sub> depth profiles for Hapludolls, Calciudolls, and Eutrudepts replotted from panel (b).

We derived an average Hapludoll carbonate depth distribution by calculating 1-cm slice-wise mean carbonate contents from the NCSS data in the AQP package in R (Beaudette et al., 2013, Figure 3). Utilizing the postsettlement component of the LODO model (section 2.6.1), we evaluated the effect of various  $E_{\text{post}}$  rates on these carbonate depth profiles and the additional depth to-or thickness-of-calcic horizons that would be required at each sampling location to minimize root-mean-square error with respect to observed CaCO<sub>3</sub> depth distributions for model predicted erosion rates. Further details of these model runs and the resulting information are provided in Text S4.

### 3. Results

#### 3.1. <sup>10</sup>Be<sub>m</sub> Relationships, Depth Distributions, and Inventories

Concentrations of <sup>10</sup>Be<sub>m,T</sub> across the studied hillslopes ranged from  $0.63 \times 10^7$  atoms/g in subsoils to  $26.8 \times 10^7$  atoms/g in topsoils at depositional sites (Table 1). The surficial <sup>10</sup>Be<sub>m,T</sub> concentrations of sampled locations ranged from a minimum of  $3.16 \times 10^7$  atoms/g on the highly eroded cultivated backslope position (5-12) to a maximum of  $26.8 \times 10^7$  atoms/g in a depositional position (2H5) on the uncultivated hillslope (Figure 4a and Table 1). Among all samples, <sup>10</sup>Be<sub>m,T</sub> concentrations were correlated with SIC concentrations ( $r = -0.56$ ,  $p < 0.001$ , Pearson's correlation coefficient), but not correlated with SOC, clay concentration, or <sup>137</sup>Cs activities. When only the surficial values of at each location are considered, SIC was an excellent predictor of surficial increment <sup>10</sup>Be<sub>m,T</sub> concentrations ( $r^2 = 0.81$ ,  $p < 0.001$ ; Figure S3). In contrast to the lack of a strong relationship with <sup>10</sup>Be<sub>m,T</sub>, SOC concentrations were good predictors of <sup>137</sup>Cs activities when all samples ( $r^2 = 0.88$ ,  $p < 0.001$ ) and surficial samples only were considered ( $r^2 = 0.88$ ,  $p < 0.001$ ; Figure S3). The resulting <sup>10</sup>Be<sub>m,I</sub> average for the study site per our algorithm (equations (1)–(3)) was  $1.07 \pm 0.31 \times 10^7$  atoms/g. When this value was applied to all cultivated locations to determine <sup>10</sup>Be<sub>m,A</sub>

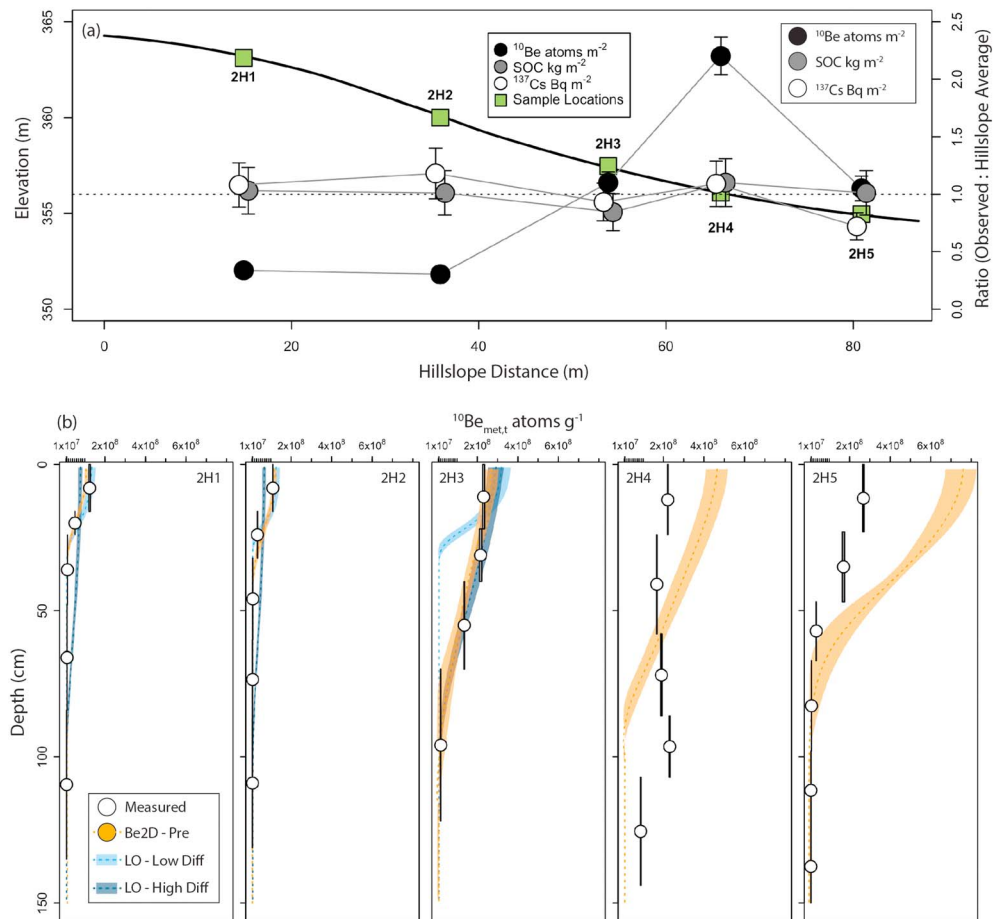


**Figure 4.** (a) Variation in  $^{10}\text{Be}_{\text{m,T}}$ , SOC, and  $^{137}\text{Cs}$  inventories across the uncultivated hillslope at locations 2H1, 2H2, 2H3, 2H4, and 2H5. The error bars on the constituent inventories represent inventory uncertainty ( $1\sigma$ ), including both analytical and bulk density uncertainties. (b) results of presettlement modeling of  $^{10}\text{Be}_{\text{m}}$  depth distributions for Be2D, LODO-low and LODO-high (in the case of LODO models, the dotted line represents the best fit model, while the error range represents the 5th–95th quantile range of prediction from 1,000 Monte Carlo runs). LODO models are not evaluated at lower slope positions 2H4 and 2H5. The error bars (colored bands) on measured  $^{10}\text{Be}_{\text{m,T}}$  increment inventories (atoms/ $\text{g}$ ) represent the concentration uncertainty ( $1\sigma$ ), from  $^{10}\text{Be}$  measurement error and span the sampling depth increment.

concentrations, only the footslope position of the cultivated transect (5-14) had  $^{10}\text{Be}_{\text{m,A}}$  remaining below the plow layer (Table 1). All other cultivated locations had  $^{10}\text{Be}_{\text{m,A}}$  remaining only in the plow layer. In contrast, uncultivated upper hillslope positions 2H1 and 2H2 contained  $^{10}\text{Be}_{\text{m,A}}$  from 24- to 32-cm depth, respectively, while the uncultivated backslope (2H3) and footslope (2H4 and 2H5) positions had  $^{10}\text{Be}_{\text{m,A}}$  to depths ranging from 67 to 144 cm below the soil surface (Figures 4a and 5a and Table 1).

The shape of  $^{10}\text{Be}_{\text{m,T}}$  depth profiles was highly dependent upon landscape position. Summit and shoulder positions on the uncultivated (2H1 and 2H2) and cultivated (5-8, 5-9, and 5-10) hillslopes as well as a back-slope position at the cultivated hillslope (5-12) exhibited decreases in  $^{10}\text{Be}_{\text{m,T}}$  concentrations with depth, (Figures 4b and 5b), typical of stable or eroding landscape positions in young landscapes where diffusion and not advection is the dominant process of the downward movement of  $^{10}\text{Be}_{\text{m}}$  in the soil profile (Graly et al., 2010; Willenbring & von Blanckenburg, 2010). In contrast, the uncultivated backslope (2H3) and all lower slope positions (5-14, 2H4, and 2H5) were cumulative in profile (Figures 4b and 5b).

Inventories of  $^{10}\text{Be}_{\text{m,T}}$  varied between land use and hillslope positions. On average,  $^{10}\text{Be}_{\text{m,T}}$  inventories to 150 cm on the cultivated hillslope were lower than those on the uncultivated hillslope ( $7.04 \pm 0.70 \times 10^{13}$  atoms/ $\text{m}^2$  and  $14.0 \pm 1.17 \times 10^{13}$  atoms  $\text{m}^2$ , respectively; Table S2). Along the uncultivated hillslope,  $^{10}\text{Be}_{\text{m,T}}$  inventories varied systematically with landscape position, with the exception of

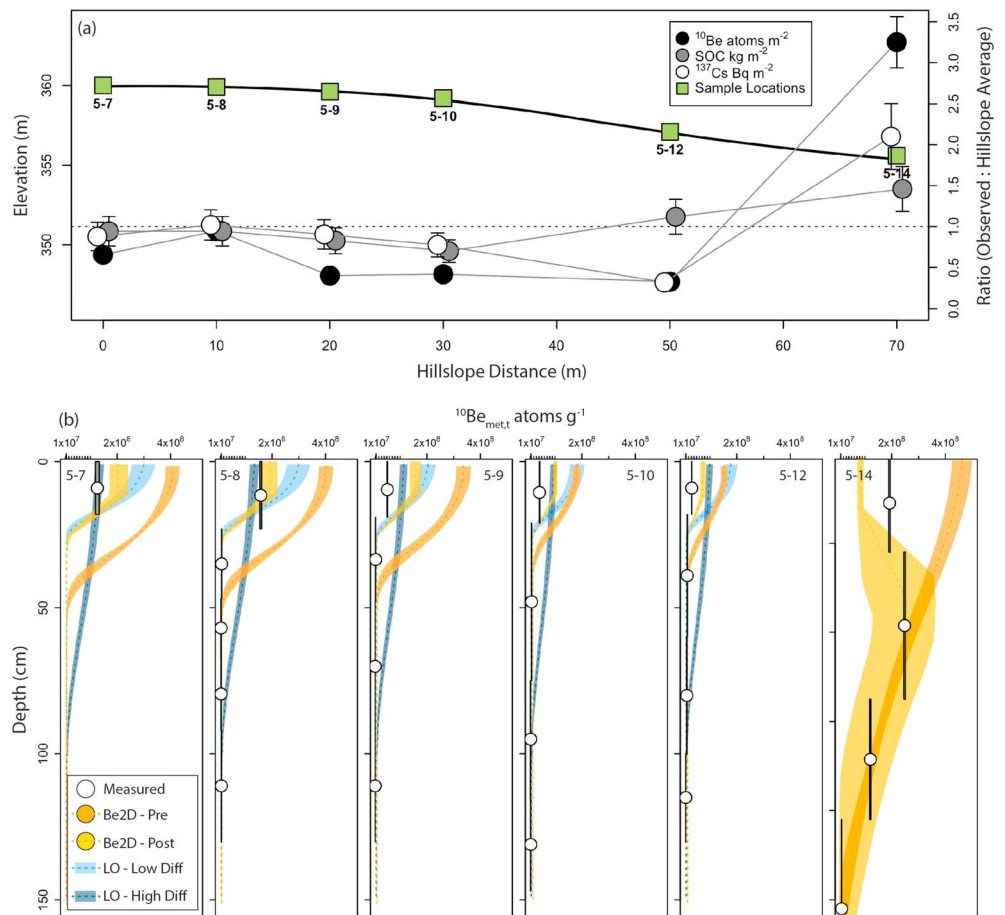


**Figure 5.** (a) Variation in  $^{10}\text{Be}_{\text{m,T}}$ , SOC, and  $^{137}\text{Cs}$  inventories across the cultivated hillslope at locations 5-7, 5-8, 5-9, 5-10, 5-11, 5-12, and 5-14. The error bars on the constituent inventories represent inventory uncertainty ( $1\sigma$ ), including both analytical and bulk density uncertainties. (b) Results of presettlement modeling of  $^{10}\text{Be}_{\text{m}}$  depth distributions for Be2D, LODO-low, and LODO-high (in the case of LODO models; the dotted line represents the best fit model, while the error range represents the 5–95th quantile range of prediction from 1,000 Monte Carlo runs). LODO models are evaluated at lower slope position 5-14. Predicted postsettlement  $^{10}\text{Be}_{\text{m}}$  distributions from the Be2D model are presented at all sampling locations. The error bars (colored bands) on measured  $^{10}\text{Be}_{\text{m,T}}$  increment inventories (atoms/g) represent the concentration uncertainty ( $1\sigma$ ), from  $^{10}\text{Be}$  measurement error and span the sampling depth increment.

location 2H5, which, although at the lowest elevation along the hillslope, had a lower inventory ( $14.8 \times 10^{13} \pm 1.5 \times 10^{13}$  atoms/ $\text{m}^2$ ) than 2H4, the location above it ( $30.9 \times 10^{13}$  atoms/ $\text{m}^2 \pm 2.3 \times 10^{13}$  atoms/ $\text{m}^2$ ). This is likely due to an artifact of tillage along the edge of a cultivated field below the uncultivated hillslope (Figure 2 and section 2.1.2).

$^{10}\text{Be}_{\text{m,A}}$  inventories were highly correlated to  $^{10}\text{Be}_{\text{m,T}}$  inventories and were lower on the cultivated hillslope than the uncultivated hillslope ( $8.14 \pm 0.83 \times 10^{13}$  atoms/ $\text{m}^2$  and  $11.8 \pm 1.08 \times 10^{13}$  atoms/ $\text{m}^2$ , respectively). On the uncultivated hillslope, total inventories of SOC and  $^{137}\text{Cs}$  did not vary by more than 30% from the hillslope average (Figure 4a), while  $^{10}\text{Be}_{\text{m,T}}$  inventories varied as much as 200% from the average (Figure 4a). In contrast, SOC,  $^{137}\text{Cs}$ , and  $^{10}\text{Be}_{\text{m,T}}$  varied by greater than 150%, 200%, and 300%, respectively, on the cultivated hillslope (Figure 5a), with most of the variability occurring at the footslope position (5-14).

### 3.2. Natural ( $E_{\text{nat}}$ ) and Postsettlement ( $E_{\text{post}}$ ) Erosion Rate Estimates: LODO and Be2D Models

The  $^{10}\text{Be}_{\text{m}}$  conversion models differed in their ability to represent observed  $^{10}\text{Be}_{\text{m}}$  depth distributions across the uncultivated hillslope. At location 2H1 and 2H2, the LODO-Low model (with  $D_{\text{s0}} = 0.2$   $\text{cm}^2/\text{year}$  and  $d_e = 5$  cm) and Be2D models best represented the observed depth profiles (Figure 4b). At 2H3, the LODO-High model (with  $D_{\text{s0}} = 0.5$  and  $d_e = 28$  cm) and Be2D best represented the observed depth profile, while

LODO-Low provided the worst fit to the observed depth distribution (Figure 4b). Both Be2D and LODO-High predicted deeper  $^{10}\text{Be}_m$  penetration into the subsurface than the LODO-Low model (Figures 4 and S4). At lower slope positions, the LODO models were not evaluated (section 2.6.1), and the Be2D model did a moderately poor job of representing the vertical  $^{10}\text{Be}_m$  profile at 2H4 (Figure 4b). However, the Be2D model was capable of reproducing the observed  $^{10}\text{Be}_{m,T}$  inventory at 2H4 (Figure S5). As we do not use the vertical  $^{10}\text{Be}_m$  distribution at 2H4 or 2H5 to calibrate either the LODO models or Be2D (Texts S2 and S3.4), this observation has little effect on the results presented here. Be2D was able to produce a reasonable pattern of soil movement by creep and water erosion processes on the uncultivated slope (Figure S6).

Predicted  $E_{\text{nat}}$  at 2H1, 2H2, and 2H3 on the uncultivated slope averaged 0.08 mm/year for LODO-Low and 0.13 mm/year for LODO-High. Be2D predicted an average erosion rate of 0.057 mm/year at the eroding locations (2H1 and 2H2) and natural soil accumulation rates ranging from  $-0.042$  to  $-0.061$  mm/year at lower slope positions 2H3, 2H4, and 2H5 (Figure S7). Be2D predicted  $E_{\text{nat}}$  to be highest at 2H1, decreasing downslope to accumulation areas, while LODO-Low and LODO-High predicted slightly higher  $E_{\text{nat}}$  at 2H2 than 2H1, due to differences in slope.

Presettlement depth distributions of  $^{10}\text{Be}_m$  predicted by the LODO models and Be2D at upper hillslope positions (5-7, 5-8, 5-9, 5-10, and 5-12) on the cultivated hillslope differed significantly (Figures 5b and S8), with the LODO-Low model predicting significantly shallower presettlement distributions of  $^{10}\text{Be}_m$  at these locations (Figure 5b).  $E_{\text{nat}}$  derived from both LODO models across the eroding positions on the cultivated hillslope (locations 5-7 to 5-12) ranged from 0.031 to 0.102 mm/year (Table 3). This resulted in expected presettlement  $^{10}\text{Be}_{m,T}$  inventories of  $5.2\text{--}8.6 \times 10^{13}$  atoms/m<sup>2</sup>, while observed modern inventories ranged from  $2.3$  to  $6.7 \times 10^{13}$  atoms/m<sup>2</sup> (Table S2).  $E_{\text{nat}}$  estimates from Be2D on the cultivated hillslope were generally lower than  $E_{\text{nat}}$  estimates from the LODO models (Figure 6 and Table 3), particularly at summit positions (5-7 and 5-8). Be2D was able to represent the observed depth distribution of  $^{10}\text{Be}_m$  at the footslope position (5-14) and predicted a lower surface concentration of  $^{10}\text{Be}_m$  due to erosion of  $^{10}\text{Be}_m$  poor materials from upslope over time (Figures 5b and S8).

LODO  $E_{\text{post}}$  estimates at cultivated locations 5-7, 5-8, 5-9, 5-10, and 5-12 ranged from 0.16 to 7.37 mm/year (Table 3), with an average  $E_{\text{post}}$  of 2.8 mm/year. LODO  $E_{\text{post}}$  estimates at shoulder and backslope positions (5-9, 5-10, and 5-12) were, on average, more than seven times those at the summit positions (5-7 and 5-8) and peaked at backslope position 5-12 (Figure 6 and Table 3). Be2D was able to generate a reasonable fit to observed  $^{10}\text{Be}_m$  inventories across the cultivated hillslope (Figure S9), as well as a reasonable representation of processes due to creep, water erosion, and tillage erosion (Figure S10). On average, Be2D  $E_{\text{post}}$  estimates were similar in magnitude to LODO  $E_{\text{post}}$  estimates, ranging from 0.25 to 4.89 mm/year, and peaked approximately 5-m downslope of the shoulder position 5-10 with an average  $E_{\text{post}}$  across eroding upper hillslope positions of  $3.27 \pm 1.14$  mm/year (Figures 6 and S11 and Table 3). However, Be2D  $E_{\text{post}}$  estimates were higher than both LODO models at summit positions 5-7 and 5-8 (Table 3).

### 3.3. $E_{\text{post}}$ From WaTEM and $^{137}\text{Cs}$ Mass Balance Models

$E_{\text{post}}$  estimates from both of the  $^{137}\text{Cs}$  Mass Balance models (MBM2 and MBM3) resulted in a pattern that differed from the other models, with the lowest  $E_{\text{post}}$  estimated at shoulder position 5-9, and the numerically highest  $E_{\text{post}}$  estimated at backslope position 5-12 (Figure 6). The  $^{137}\text{Cs}$  MBM2 conversion model resulted in soil loss estimates of 1.67 to 5.15 mm/year at summit, shoulder, and backslope positions (Table 3) and a rate of 0.18 mm/year at the cultivated footslope position (5-14). The  $^{137}\text{Cs}$  MBM3 model resulted in soil loss estimates ranging from 2.01 to 5.86 mm/year at summit, shoulder, and backslope positions (Table 3) and a rate of 0.21 mm/year at the footslope position (5-14). Both  $^{137}\text{Cs}$  conversion models resulted in similar patterns of predicted erosion rates across the hillslope, with a peak at the backslope position 5-12 (Figure 6).

### 3.4. Model Suite Intercomparison

When all sampling locations were considered, Be2D  $E_{\text{post}}$  estimates were not significantly different, on average, than either of the LODO models, the  $^{137}\text{Cs}$  proportion models (both MBM2 and MBM3), or WaTEM (paired  $t$  tests with Holm's correction for multiple comparisons,  $p > 0.1$  in all cases; Table 3).  $E_{\text{post}}$  estimates from both LODO models were highly correlated due to their structural similarity ( $r = 0.99$ ,  $p < 0.001$ , Pearson's correlation coefficient), but were not correlated to any of the other models.

**Table 3**  
Erosion Estimates at Cultivated Sampling Locations for a Suite of Conversion Models

Location	Hillslope position	Presettlement models ( $E_{nat}$ )				Postsettlement models ( $E_{post}$ )						
		LODO-Low <sup>a</sup> (mm/year)	LODO-High <sup>b</sup> (mm/year)	Be2D (mm/year)	Average <sup>c</sup> (mm/year)	LODO-low <sup>b</sup> (mm/year)	LODO-high (mm/year)	Be2D (mm/year)	<sup>137</sup> Cs MBM2 <sup>d</sup> (mm/year)	<sup>137</sup> Cs MBM3 <sup>d</sup> (mm/year)	WaTEM (mm/year) <sup>e</sup>	Average <sup>c</sup> (mm/year)
5-7	Summit	0.031 <sup>f</sup>	0.055	0.0044 ± 0.0008	0.030 ± 0.025 Aa	0.60 ± 0.30 <sup>g</sup>	1.13 ± 0.38	2.17 ± 0.30 <sup>g</sup>	2.48 ± 1.24	4.89 ± 1.56	3.22	2.42 ± 1.54 Ba
5-8	Summit	0.031	0.056	0.0042 ± 0.0008	0.030 ± 0.026 Aa	0.16 ± 0.17	0.32 ± 0.19	2.28 ± 0.29	2.20 ± 1.16	2.01 ± 1.28	2.96	1.66 ± 1.14 Ba
5-9	Shoulder	0.036	0.064	0.01 ± 0.003	0.037 ± 0.027 Aa	2.25 ± 0.54	5.31 ± 1.39	3.16 ± 0.28	1.67 ± 0.80	1.45 ± 0.80	3.31	2.86 ± 1.42 Bab
5-10	Shoulder	0.051	0.091	0.054 ± 0.006	0.065 ± 0.022 Aa	2.30 ± 0.57	5.14 ± 1.37	4.89 ± 0.63	2.27 ± 1.00	2.46 ± 1.02	4.53	3.60 ± 1.39 Bab
5-12	Backslope	0.057	0.102	0.059 ± 0.009	0.073 ± 0.025 Aa	3.18 ± 0.69	7.37 ± 1.89	3.87 ± 1.54	5.15 ± 2.18	5.86 ± 2.20	4.08	4.92 ± 1.78 Bb
Upper Slope Locations, Average (5-7 and 5-12) <sup>h</sup>		0.041 ± 0.012 A	0.070 ± 0.021 B	0.026 ± 0.028 A	0.047 ± 0.020	1.70 ± 1.27 C	3.85 ± 3.00 C	3.27 ± 1.14 C	2.75 ± 1.37 C	3.33 ± 1.93 C	3.62 ± 0.66 C	3.09 ± 1.11
5-14	Footslope	— <sup>i</sup>	—	−0.071 ± 0.011 <sup>h</sup>	−0.071	—	—	0.25 ± 1.92	0.18 ± 0.66	0.21 ± 1.78	0.51	0.29 ± 0.15 c

<sup>a</sup>Loss only, diffusion only (LODO)-Low diffusion case. <sup>b</sup>Loss only, diffusion only (LODO)-High diffusion case. <sup>c</sup>Numbers reported in the Average columns are the arithmetic mean and standard deviation of all model outputs at a given location for either the pre-settlement ( $E_{nat}$ ) or postsettlement ( $E_{post}$ ) case. Locations with different capital letters for the  $E_{nat}$  and  $E_{post}$  average columns have groups of erosion rate estimates that are significantly different (Tukey's honestly significant difference,  $p < 0.001$  in all cases). Locations with different lowercase letters within a column have erosion rate estimates that are significantly different (paired  $t$  test with Holm's correction for multiple comparisons,  $p < 0.05$ ). <sup>d</sup>Results reported for the mass balance model 2 (MBM2) and mass balance model 3 (MBM3). <sup>e</sup><sup>137</sup>Cs conversion models are the mean and standard deviation ( $1\sigma$ ) of 18 model runs utilizing a range of <sup>137</sup>Cs reference inventories and parameter values as detailed in Table S3. <sup>f</sup>Estimated post settlement erosion rate ( $E_{post}$ ) from Water and Tillage Erosion Model (WaTEM; van Oost et al., 2000) from Papernik et al. (2005). <sup>g</sup>Minimum root-mean-square error solution for average natural erosion rate ( $E_{nat}$ ) from numerical model. <sup>h</sup>Reported uncertainty for LODO and Be2D models represents the 5th to 95th percentile of 1,000 Monte Carlo simulations. <sup>i</sup>Numbers reported in the Upper Slope Locations Average row are the arithmetic mean and standard deviation of locations 5-7, 5-8, 5-9, 5-10, and 5-12 for a given model. Capital letters indicate groups of erosion rate estimates that are significantly different (paired  $t$  test with Holm's correction for multiple comparisons,  $p < 0.05$ ). <sup>j</sup>Negative values (−) represent accumulation rate estimates at footslope position (5-14). LODO models are not applied at accumulation positions.

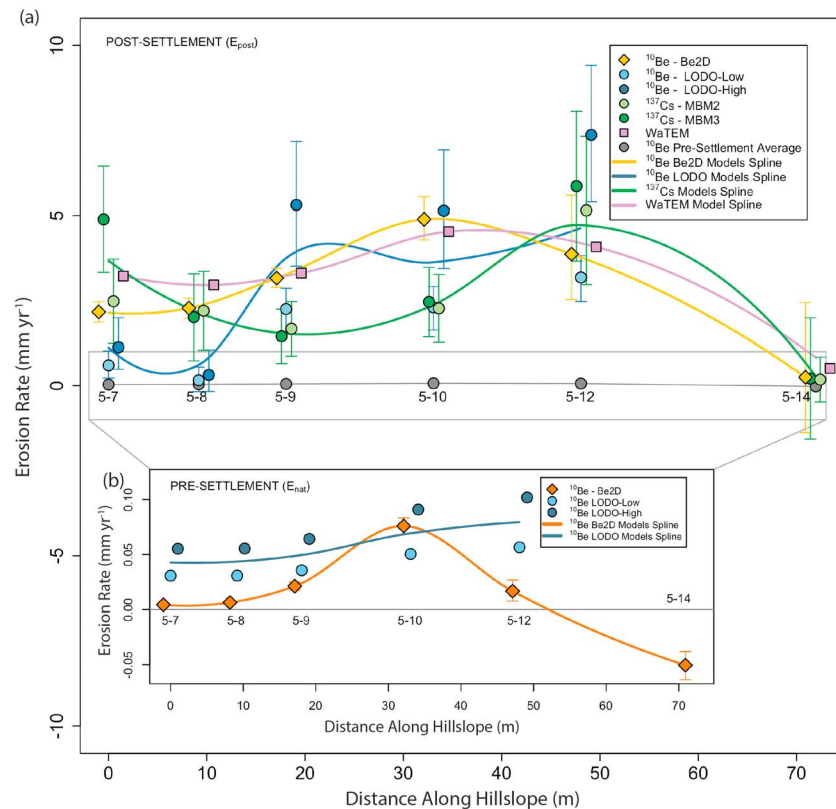


**Figure 6.** Erosion rate estimates across the cultivated hillslope for all models. (a) Postsettlement erosion rate ( $E_{post}$ ) estimates for the suite of models. Uncertainties for the loss only, diffusion only (LODO), and <sup>137</sup>Cs mass balance models are presented as in Table 3. For visualization purposes for the LODO and <sup>137</sup>Cs models, a spline is fit through the average results at each sampling location from both predictions. Inset (b): Presettlement (natural) erosion rate estimates across the cultivated hillslope for the LODO and Be2D models.

No differences between hillslope positions for  $E_{nat}$  estimates were apparent (Tukey's honestly significant difference,  $p > 0.1$ ) when erosion estimates from all models were considered (Table 3). For  $E_{post}$ , however, erosion rate estimates for all models at the backslope (5-12) position ( $4.92 \pm 1.78$  mm/year) were significantly higher than erosion rates estimates at either of the summit positions (5-7 and 5-8;  $2.42 \pm 1.54$  mm/year and  $1.66 \pm 1.14$  mm/year, respectively).  $E_{post}$  estimates at the footslope position (5-14) for Be2D, <sup>137</sup>Cs MBMs, and WaTEM were significantly lower ( $0.29 \pm 0.15$  mm/year) than  $E_{post}$  estimates across all other hillslope positions on the cultivated slope (Table 3).

Modeled patterns of  $E_{post}$  differed across the hillslope (Figure 6). Both Be2D and WaTEM erosion rate estimates peaked near the shoulder position 5-10, while LODO-Low, LODO-High, and both <sup>137</sup>Cs conversion models (MBM2 and MBM3) peaked at backslope position 5-12. At the footslope position 5-14, all models (except the LODO models, which were not evaluated at lower slope positions) strongly converged (Figure 6). At footslope position 5-14, MBM2, MBM3, and WaTEM all predicted low-magnitude net erosion. Be2D predicted an erosion rate of  $0.25 \pm 1.92$  mm/year (the high uncertainty of the model prediction at this location is also reflected in the large uncertainty in the depth distribution (Figure 5b), but this estimate is broadly convergent with <sup>137</sup>Cs MBM and WaTEM models, all of which predicted low net erosion (ranging from 0.18 to 0.51 mm/year) at that location (Table 3).

### 3.5. Relationship of <sup>10</sup>Be Erosion Rate Estimates to Evidence From Carbonate Depth Distributions

Figure 3c shows the depth distributions of CaCO<sub>3</sub> equivalent at all six cultivated sampling locations. Summit position 5-8 has not yet eroded into the calcic horizon and matches the NCSS Hapludoll average depth distribution well, while locations 5-7 and 5-9 show erosion into the calcic horizon (elevated surface CaCO<sub>3</sub> but retaining a CaCO<sub>3</sub> peak in the subsurface). In contrast, location 5-10 appears to be eroded completely

through the calcic horizon and into the parent material (Figure 3c). Therefore, from  $\text{CaCO}_3$  distributions alone, and assuming equal presettlement depth distributions of carbonates, the magnitude of erosion and apparent soil truncation due to erosion increases in the following order: 5-14 < 5-8 < 5-7 < 5-9 < 5-12 < 5-10. This broadly matches patterns in  $E_{\text{post}}$  magnitude predicted by our models (Figure 6 and Table 3).

Utilizing the range of predicted calcic horizon depths and thickness for our study site based on climatic relationships from other sources (Retallack, 2005; Yaalon, 1983), in combination with results from the postsettlement erosion and mixing model on the Hapludoll profile, enabled us to provide first-order constraints on the likelihood of various  $E_{\text{post}}$  estimates in the context of carbonate profiles (Figure S12 and Table S6). With the exception of shoulder position 5-10 (which has been eroded completely through the calcic horizon into the parent material), all of the  $^{10}\text{Be}$  conversion models (LODO-Low, LODO-High, and Be2D) required only modest additions of depth to and or thickness of the calcic horizon of the average Hapludoll profile to obtain reasonable model fits (Figures 3c and S12 and Table S6).

## 4. Discussion

### 4.1. Relationship of $^{10}\text{Be}_m$ Observations to Previous Studies in Regional Agricultural Landscapes

The average of surficial  $^{10}\text{Be}_{m,T}$  concentrations reported in previous studies in Minnesota and Iowa ( $n = 11$ ) is  $20.9 \times 10^7$  atoms/g (Balco, 2004; Belmont et al., 2011; Harden et al., 2002). While the surficial  $^{10}\text{Be}_m$  concentrations on our uncultivated hillslope are broadly congruent with these previous values ( $19.1 \pm 7.0 \times 10^7$  atoms/g), the surficial concentrations of  $^{10}\text{Be}_{m,T}$  on the cultivated hillslope ( $10.1 \pm 6.8 \times 10^7$  atoms/g) are lower. This concentration difference alone suggests that the cultivated hillslope has lost a significant amount of soil relative to sites investigated in these previous studies. Values of  $^{10}\text{Be}_{m,I}$  at our study site (ranging from  $0.88 \times 10^7$  atoms/g to  $1.26 \times 10^7$  atoms/g) are similar to  $^{10}\text{Be}_m$  concentrations reported in deep deposits of unweathered Des Moines lobe till from the banks of the Minnesota River ( $0.8 \times 10^7$  atoms/g; Belmont et al., 2011) and inherited values from below 1 m in Des Moines lobe till ( $1.9 \times 10^7$  atoms/g) on a roadcut near Henderson, Minnesota (Balco, 2004).

While  $^{10}\text{Be}_m$  inventories varied by more than 200% across the uncultivated hillslope, SOC inventories varied by less than 30% and were not related to hillslope position, suggesting that the soil movement recorded by  $^{10}\text{Be}_m$  on the uncultivated slope is related to long-term processes and not recent or episodic deposition events. If agricultural activities postsettlement had significantly altered soil movement along the uncultivated hillslope, we would expect to see a significant increase in SOC inventories downslope associated with postsettlement soil erosion and deposition (Papiernik et al., 2005; Quine & van Oost, 2007; van Oost et al., 2012). This is in strong contrast to  $^{10}\text{Be}_m$  and SIC inventories, which exceeded 150 and 300% variation around the average across the uncultivated hillslope, indicating their responsiveness to processes operating over time periods relevant to soil formation.

### 4.2. Relationship of Model Parameter and Erosion Rate Estimates to Previous Studies

The surficial diffusion constant ( $D_{s0}$ , 0.2–0.5  $\text{cm}^2/\text{year}$ ) and  $e$ -folding depth ( $d_e$ , 5–28 cm) parameters derived for the uncultivated hillslope in our LODO models are within the range of those reported in structurally similar models using  $^{10}\text{Be}_m$  and  $^7\text{Be}$ . Using  $^{10}\text{Be}_m$ , Jagercikova et al. (2017) estimated a  $D_{s0}$  of 3.2  $\text{cm}^2/\text{year}$  and  $d_e$  of 33 cm for an uncultivated grassland soil formed in loess, while Johnson et al. (2014) estimated  $D_{s0}$  values of 1.8–2.1  $\text{cm}^2/\text{year}$  and a  $d_e$  value of 28 cm in an Australian open savanna woodland. Kaste et al. (2007) used  $^7\text{Be}$  to estimate surficial diffusion constants of 0.2 to 2.4  $\text{cm}^2/\text{year}$  across a range of natural ecosystems. The surficial diffusion constant ( $D_{s0,B}$  0.74  $\text{cm}^2/\text{year}$ ) and  $e$ -folding depth ( $d_e = 1/b_D$ , 9.1 cm; equation (S2)) parameters derived for the uncultivated hillslope in the Be2D model are also within the range of the above reported values. Note that there exist tradeoffs between model parameter values used in Be2D (Table S4). An example of this interdependency is a positive correlation between values for diffusion ( $D_{s0,B}$ ) and the sorption coefficient ( $K_D$ ). The higher the value for  $K_D$ , the more  $^{10}\text{Be}_m$  will be tightly sorbed to the upper soil layers and the higher  $D_{s0,B}$  must be to obtain vertical mixing of the same magnitude. Other possible parameter interdependencies are evaluated through a series of synthetic model runs in Campforts et al. (2016) and Figure 6 therein.

Under these parameters,  $^{10}\text{Be}_m$  would have been largely absent below 1 m on stable landscape positions and upper hillslope positions prior to human disturbance. This is reasonable at our study site because  $^{10}\text{Be}_m$  is likely to be largely immobile and therefore only transported downward from the surface through diffusion-like processes such as bioturbation. Accordingly, based on our inheritance assumptions, no  $^{10}\text{Be}_{m,A}$  was observed below 1 m at sampling locations experiencing net soil loss (5-7, 5-8, 5-9, 5-10, 5-12, 2H1, and 2H2) at our study site, regardless of land use (Figures 4b and 5b and Table S2). In other landscapes where advective processes such as clay illuviation or loess accumulation become more important,  $^{10}\text{Be}_{m,A}$  can be observed well below 1-m depth (Bacon et al., 2012; Balco, 2004; Harden et al., 2002; Johnson et al., 2014).

Our  $^{10}\text{Be}_m$ -derived estimates of  $E_{\text{nat}}$  for eroding locations on both hillslopes (ranging from 0.0044 to 0.102 mm/year on the cultivated hillslope and 0.01 to 0.19 mm/year on the uncultivated hillslope) are within the global range of natural erosion rates expected for soil-mantled landscapes (Montgomery, 2007; Nearing et al., 2017) and are comparable to  $E_{\text{nat}}$  derived for a single location from  $^{10}\text{Be}_m$  for a loess-mantled back-slope under grassland vegetation in Iowa (0.03–0.13 mm/year; Harden et al., 2002). These  $E_{\text{nat}}$  rates are 1 to 2 orders of magnitude higher than  $E_{\text{nat}}$  derived from  $^{10}\text{Be}_m$  under steady state assumptions on stable positions in older landscapes (0.00035–0.038 mm/year; Bacon et al., 2012; Johnson et al., 2014; Lal et al., 2012; Schoonejans et al., 2017) and are slightly higher in magnitude than long-term erosion rates of soils formed in shale residuum on narrow interfluvies in the northern Appalachian mountains of central Pennsylvania, USA (0.016–0.019 mm/year; West et al., 2013). These results are reasonable, given that the soils at our study site are formed from deep, unconsolidated parent materials, were likely heavily bioturbated prior to agricultural conversion, and were exposed to high-frequency fire regimes in a humid climate.

$E_{\text{post}}$  estimates derived only from  $^{10}\text{Be}_m$  conversion models across all upper hillslope positions (5-7, 5-8, 5-9, 5-10, and 5-12) on the cultivated hillslope ( $2.94 \pm 2.07$  mm/year—not aggregated in Table 3) were also within the range of erosion rates reported for agricultural landscapes around the world (Garcia-Ruiz et al., 2015; Montgomery, 2007). In previous work at our study site, maximum point-based erosion rates derived from  $^{137}\text{Cs}$  inventories and process-based models (WaTEM and TillTM) evaluated on a sampling grid across the 2.7-ha field containing the cultivated hillslope reached 6 to 10 mm/year (Li et al., 2007; Papiernik et al., 2005). Because we used the uncultivated site for model calibration and parameterization of the  $^{10}\text{Be}_m$  conversion models, if human disturbance at any time accelerated erosion on the uncultivated site, our  $E_{\text{post}}$  estimates on the cultivated hillslope would underestimate the true postsettlement erosion rate.

Given the large difference in timescales at which we derive estimates of  $E_{\text{nat}}$  (13,000 years) and  $E_{\text{post}}$  (110 years) on the cultivated hillslope, we must consider the potential impact of apparent decreasing rates of denudation with increasing measurement interval (i.e., the *Sadler effect*; Sadler, 1981, 1994) on the significantly higher  $E_{\text{post}}$  rates. In order to evaluate the potential impact of this effect on our interpretation of the results presented in this study, we transformed our average  $E_{\text{nat}}$  ( $0.047 \pm 0.020$  mm/year) and  $E_{\text{post}}$  ( $3.09 \pm 1.11$  mm/year) rates from eroding positions on the cultivated hillslope to standardized yearly depths using the regression equations developed for landscape denudation in Gardner et al. (1987). The standardized yearly depths for these hillslope-average erosion rates became 0.27 mm for  $E_{\text{pre}}$  and 7.40 mm for  $E_{\text{post}}$ . Thus, it appears that while the Sadler effect may explain a portion of the difference in estimated  $E_{\text{nat}}$  and  $E_{\text{post}}$  values across the cultivated site, our interpretation of the results as indicating a 1 to 2 order of magnitude increase in erosion rates on upper hillslope positions following European settlement at this study site remains robust.

### 4.3. Implications of Model Selection on $E_{\text{post}}$ Estimates

Despite the general agreement of our  $^{10}\text{Be}_m$   $E_{\text{post}}$  estimates with previous work, important differences between models exist. Both LODO models are structurally equivalent and bracket a range of  $E_{\text{post}}$  uncertainty reflective of underlying uncertainties in diffusion coefficients. However, these models treat each location independently, and although they produce  $E_{\text{post}}$  estimates of reasonable magnitude, unlike Be2D they do not reflect process-based patterns on the landscape. For example, whereas both Be2D and WaTEM predict a peak in erosion rate near shoulder position 5-10 (convex shoulder) followed by a decrease at 5-12 (linear backslope) the LODO models cannot reasonably reproduce this pattern (Figure 6), and thus, the results from the LODO models should be viewed with high skepticism in locations where net sediment flux is low.

All models, which are valid at the footslope position 5-14 (WaTEM, Be2D, MBM2, and MBM3), predicted that sampling location 5-14 has experienced low-magnitude net erosion postsettlement, likely due to the combined effects of both tillage and water erosion. WaTEM predicts that 5-14 is a depositional location with respect to tillage erosion ( $-0.5$  mm/year), and an eroding position with respect to water erosion (1.0 mm/year), suggesting that there is actually net erosion occurring over the long term at this position (Table 3), due to the location of footslope position 5-14 in an upland drainageway (Papiernik et al., 2005). Be2D also captures this dynamic (Figure S10), and estimates of total erosion from  $^{137}\text{Cs}$  (MBM2 and MBM3) were similar to Be2D and WaTEM (Figure 6 and Table 2).

#### 4.4. Implications of $^{10}\text{Be}_m$ Erosion Rate Estimates on Understanding of Post-European Settlement Landscape Change

The values of our  $^{10}\text{Be}_m$   $E_{\text{post}}$  estimates on the cultivated hillslope suggest several different scenarios with regard to temporal changes in erosion rates. When all  $^{10}\text{Be}_m$  models are considered, it is likely that relative to  $E_{\text{nat}}$  ( $0.047 \pm 0.020$  mm/year), erosion rates on the cultivated hillslope have increased by approximately 2 orders of magnitude (to  $3.09 \pm 1.11$  mm/year) under postsettlement agricultural land use. If these  $^{10}\text{Be}_m$   $E_{\text{post}}$  estimates represent a 110-year average erosion rate and the  $^{137}\text{Cs}$  and WaTEM erosion rates are considered to represent typical erosion rates over the past  $\sim 53$  years or current conditions, we can qualitatively evaluate relative changes in *early* and *late* postsettlement erosion rates. The average of these modern erosion rate estimates ( $^{137}\text{Cs}$  mass balance models and WaTEM) across eroding positions on the cultivated hillslope is  $3.24 \pm 1.36$  mm/year. When compared to 110-year  $E_{\text{post}}$  from  $^{10}\text{Be}_m$  models, we reach the conclusion that erosion rates ( $3.24$  vs  $2.94$  mm/year for  $^{137}\text{Cs}$ /WaTEM and  $^{10}\text{Be}_m$  models, respectively) may not have not significantly changed from early to late postsettlement agricultural land use at this particular site. This result is reasonable at our study site, given the competing directions of change on  $E_{\text{post}}$  imposed by (1) progressively subdued topography as the landscape erodes (which would tend to result in lower  $E_{\text{post}}$  with time, e.g., van der Meij et al., 2017), (2) increases in erosion rates with mechanization (implement velocities would have been slower at the time of settlement due to use of animal power), and (3) relatively consistent tillage practices (moldboard plow was utilized for at least the 40-year-period preceding sampling in 2007 CE and likely was the major tillage implement used early postsettlement). Conversely, if conservation practices had improved, we might expect more modern erosion rate estimates to be lower than long-term average rates. Although we find no evidence in our  $E_{\text{post}}$  estimates to suggest this scenario at our particular study site, it is important to note that the uncertainties around  $E_{\text{post}}$  estimates are large, and therefore, our ability to detect differences over various timescales postsettlement is highly limited.

## 5. Conclusions

In this study, we utilized two  $^{10}\text{Be}_m$  conversion models to derive both presettlement (natural) and postsettlement erosion rates across a cultivated hillslope in west-central Minnesota, USA., revealing orders of magnitude changes in erosion rates coupled to land use change. The general convergence of our  $^{10}\text{Be}_m$  results from two independent numerical models with those of more traditional approaches from process-based models (WaTEM) or other isotopic tracers ( $^{137}\text{Cs}$ ) is encouraging and suggests that  $^{10}\text{Be}_m$  may be useful in other settings for constraining spatially explicit erosion rates under the influence of agricultural disturbance. Previous work on the Be2D model has shown that it can be applied to a range of diverse natural systems (Campforts et al., 2016); however, this is the first use of that model with data from an agricultural system. Therefore, additional studies that explore the usefulness of the Be2D model in other agricultural systems should be encouraged.

Due to a high level of measurement effort and expense relative to process-based models or other radionuclide tracers that can be readily quantified on alpha- and gamma-spectrometers such as  $^{137}\text{Cs}$  and  $^{210}\text{Pb}$ , it is unlikely that  $^{10}\text{Be}_m$  would be used in isolation to produce point-estimates of erosion rates in agricultural landscapes. Nevertheless, our work demonstrates that  $^{10}\text{Be}_m$  can be effectively utilized as an independent tracer of erosion in conjunction with more traditional approaches and that  $^{10}\text{Be}_m$  can be utilized to extend the timeframes under consideration when estimating erosion rates. These methods are likely to work best at a study site such as the one presented here, where precipitation is moderate,

surficial materials (such as the glacial till at our study site) are not highly weathered, and soil materials have high affinity with respect to  $^{10}\text{Be}$ .

## Notation

Note that generalized dimensional units for length ( $L$ ), mass ( $M$ ), and time ( $t$ ) are used in variable definitions in this list and in the text above. When numerical values are discussed, specific units are utilized.

$^{10}\text{Be}_{m,A}$	accumulated meteoric beryllium-10
$^{10}\text{Be}_{m,I}$	inherited meteoric beryllium-10
$^{10}\text{Be}_{m,T}$	total meteoric beryllium-10
$^{137}\text{Cs}_{\text{REF}}$	cesium-137 reference inventory [ $\text{Bq}/\text{m}^2$ ] ( $^{137}\text{Cs}$ MBMs)
A	annual average soil loss [ $\text{M} \cdot \text{L}^{-2} \cdot \text{t}^{-1}$ ] (RUSLE)
$b_D$	depth rate constant for diffusion (equivalent to $1/d_e$ ) [ $\text{L}^{-1}$ ] (Be2D)
Be2D	Spatially explicit two-dimensional model simulating the behavior of $^{10}\text{Be}_m$ on a hillslope (Campforts et al., 2016)
C	crop erosivity factor (RUSLE)
$C_{\text{Be}}$	soil concentration of $^{10}\text{Be}_m$ [atoms/M] (LODO and Be2D)
d	depth from soil surface ( $h - z$ ) [L]
$d_e$	$e$ -folding depth [L] (LODO)
$d_m$	mass plow depth [ $\text{M}/\text{L}^2$ ] ( $^{137}\text{Cs}$ MBMs)
$d_{\text{till}}$	tillage depth [L]
$D_s$	diffusion constant [ $\text{L}^2/\text{t}$ ] (LODO and Be2D)
$D_{s0}$	surficial diffusion constant [ $\text{L}^2/\text{t}$ ] (LODO)
$D_{s0,B}$	surficial diffusion constant [ $\text{L}^2/\text{t}$ ] (Be2D)
$E_{\text{nat}}$	matural (presettlement) erosion rate [L/t]
$E_{\text{post}}$	post-settlement erosion rate [L/t]
h	elevation of soil surface [L]
$H_{\text{MBM}}$	relaxation mass depth [ $\text{M}/\text{L}^2$ ] ( $^{137}\text{Cs}$ MBMs)
$I_A$	accumulated, noninherited $^{10}\text{Be}$ inventory [atoms $\text{L}^2$ ]
$k_{\text{till}}$	tillage transport coefficient [M/L] (WATEM)
K	soil erodibility factor [tons hr $\text{MJ}^{-1}/\text{mm}$ ] (RUSLE)
$K_D$	partition coefficient for clay [ $\text{L}^3/\text{M}$ ] (Be2D)
LODO	one-dimensional Loss-Only, Diffusion-Only model of $^{10}\text{Be}_m$ profile evolution
LODO-Low	low-diffusion case of LODO model
LODO-high	high diffusion case of LODO model
LS	slope-length factor [L/L] (RUSLE)
MBM2	$^{137}\text{Cs}$ mass balance model 2 (Walling et al., 2002)
MBM	$^{137}\text{Cs}$ mass balance model 3 (Walling et al., 2002)
$M_{10\text{Be}}$	molar mass of $^{10}\text{Be}$ [kg/mol]
$M_i$	modeled $^{10}\text{Be}_m$ concentration or inventory (Nash-Sutcliffe coefficient)
$N_A$	Avogadro's number
nb	number of observations (Nash-Sutcliffe coefficient)
NCSS	U.S. National Cooperative Soil Survey
NS	Nash Sutcliffe coefficient (Nash & Sutcliffe, 1970)
$O_i$	observed $^{10}\text{Be}_m$ concentration or inventory (Nash-Sutcliffe coefficient)
P	erosion control practice factor (RUSLE)
$P_{\text{Be}}$	$^{10}\text{Be}_m$ deposition rate [atoms $\text{L}^2$ ]
PM	$^{137}\text{Cs}$ Proportional Model (Walling et al., 2002)
$Q_{s,t}$	net soil flux due to tillage erosion [ $\text{M} \text{L}^2/\text{L}^3$ ] (WATEM)
R	Rainfall erosivity [ $\text{MJ} \text{mm} \cdot \text{hr}^{-1} \cdot \text{ha}^{-1} \text{year}^{-1}$ ] (RUSLE)
RUSLE	Revised Universal Soil Loss Equation (Renard et al., 1997)

S	slope tangent (dh/dx)
SIC	soil inorganic Carbon
SOC	soil organic carbon
SSA	specific surface area
SSA <sub>ds</sub>	specific surface area of deposited sediment [L <sup>2</sup> /M] ( <sup>137</sup> Cs MBMs)
SSA <sub>ms</sub>	specific surface area of mobilized sediment [L <sup>2</sup> /M] ( <sup>137</sup> Cs MBMs)
SSA <sub>sl</sub>	specific surface area of topsoil [L <sup>2</sup> /M] ( <sup>137</sup> Cs MBMs)
t	time [t]
T	total length of model run [t]
WaTEM	Process-based <u>W</u> ater and <u>T</u> illage <u>E</u> rosion <u>M</u> odel (van Oost et al., 2000)
WRB	World Reference Base for soils (IUSS Working Group WRB, 2015)
x	longitudinal distance along hillslope [L]
z	absolute elevation (above sea level) [L]
γ <sub>MBM</sub>	proportion of <sup>137</sup> Cs input susceptible to erosion ( <sup>137</sup> Cs MBMs)
ψ	particle size correction factor for eroding sediment ( <sup>137</sup> Cs MBMs)
ψ'	particle size correction factor for deposited sediment ( <sup>137</sup> Cs MBMs)
ρ <sub>b</sub>	soil bulk density [M/L <sup>3</sup> ]
φ	Tillage transport coefficient ( <sup>137</sup> Cs MBM3)
ν	Particle size selection factor constant ( <sup>137</sup> Cs mass balance models)

#### Acknowledgments

The authors would like to thank J. A. Schumacher, Research Engineer for assistance in setting up transects, georeferencing, detailed mapping, and field collection; D.D. Malo for assistance in soil morphological description and sampling; J. K. Willenbring acknowledges NSF grant 1651243; Purdue University's PRIME Lab and the National Science Foundation for AMS facilities and <sup>10</sup>Be measurements, University of Minnesota Grant-in-Aid 22239 to K. Yoo and an NSF Graduate Research Fellowship to N. A. Jelinski. B. Campforts received a postdoctoral grant from the Research Foundation Flanders (FWO), and computational resources and services used to run the Be2D simulations were provided by the VSC (Flemish Supercomputer Center), managed by the Research Foundation-Flanders (FWO) in partnership with five Flemish University associations. The authors would like to thank several anonymous reviews, Associate Editors, and Editors-in-Chief for highly constructive comments on several manuscript versions. The authors declare no conflicts of interest. All original data used to produce figures are available in tables provided in the supporting information associated with this article.

#### References

- Abrahams, E. R., Kaste, J. M., Ouimet, W., & Dethier, D. (2018). Asymmetric hillslope erosion following wildfire in Fourmile Canyon, Colorado. *Earth Surface Processes and Landforms*, 43(9), 2009–2021. <https://doi.org/10.1002/esp.4348>
- Bacon, A. R., Richter, D. d B., Bierman, P. R., & Rood, D. H. (2012). Coupling meteoric <sup>10</sup>Be with pedogenic losses of <sup>9</sup>Be to improve soil residence time estimates on an ancient North American interfluvium. *Geology*, 40(9), 847–850. <https://doi.org/10.1130/G33449.1>
- Baker, D. G., Nelson, W. W., & Kuehnast, E. L. (1979). Climate of Minnesota: Part XII—The hydrologic cycle and soil water. University of Minnesota Agricultural Experiment Station, Technical Bulletin 322.
- Balco, G. A. (2004). The sedimentary record of subglacial erosion beneath the Laurentide Ice Sheet. Ph.D. Dissertation, University of Washington.
- Basher, L. R., Mathews, K. M., & Zhi, L. (1995). Surface erosion assessment in the South Canterbury Downlands, New Zealand using <sup>137</sup>Cs distribution. *Australian Journal of Soil Research*, 33(5), 787–803. <https://doi.org/10.1071/SR950787>
- Beaudette, D. E., Roudier, P., & O'Geen, A. T. (2013). Algorithms for quantitative pedology: A toolkit for soil scientists. *Computers & Geosciences*, 52, 258–268. <https://doi.org/10.1016/j.cageo.2012.10.020>
- Belmont, P., Gran, K. B., Schottler, S. P., Wilcock, P. R., Day, S. S., Jennings, C., et al. (2011). Large shift in source of fine sediment in the upper Mississippi river. *Environmental Science and Technology*, 45(20), 8804–8810. <https://doi.org/10.1021/es2019109>
- Boschi, V., & Willenbring, J. K. (2016). The effect of pH, organic ligand chemistry and mineralogy on the sorption of beryllium over time. *Environmental Chemistry*, 13(4), 711–722. <https://doi.org/10.1071/EN15107>
- Brown, L., Pavich, M., Hickman, R. E., Klein, J., & Middleton, R. (1988). Erosion of the eastern United States observed with <sup>10</sup>Be. *Earth Surface Processes and Landforms*, 13(5), 441–457. <https://doi.org/10.1002/esp.3290130509>
- Brunauer, S., Emmett, P. H., & Teller, E. (1938). Adsorption of gases in multimolecular layers. *Journal of the American Chemical Society*, 60(2), 309–319. <https://doi.org/10.1021/ja01269a023>
- Bunzl, K., Kracke, W., Schimmack, W., & Auerswald, K. (1995). Migration of fallout <sup>239</sup>+<sup>240</sup>Pu, <sup>241</sup>Am and <sup>137</sup>Cs in the various horizons of a forest soil under pine. *Journal of Environmental Radioactivity*, 28(1), 17–34. [https://doi.org/10.1016/0265-931X\(94\)00066-6](https://doi.org/10.1016/0265-931X(94)00066-6)
- Campforts, B., & Govers, G. (2015). Keeping the edge: A numerical method that avoids knickpoint smearing when solving the stream power law. *Journal of Geophysical Research: Earth Surface*, 120, 1189–1205. <https://doi.org/10.1002/2014JF003376>
- Campforts, B., Vanacker, V., Vanderborgh, J., Baken, S., Smolders, E., & Govers, G. (2016). Simulating the mobility of meteoric <sup>10</sup>Be in the landscape through a coupled soil-hillslope model (Be2D). *Earth and Planetary Science Letters*, 439, 143–157. <https://doi.org/10.1016/j.epsl.2016.01.017>
- Chapman, A. S. (2001). Particulate phosphorus loss from agricultural land in the UK. PhD dissertation, Coventry University.
- Chen, P., Yu, Z. B., Aldahan, A., Yi, P., Possner, G., & Mugwanya, V. d P. (2017). Comparison of measurement and modeling results of the global <sup>10</sup>Be flux in topsoil. *Journal of Radioanalytical and Nuclear Chemistry*, 311(3), 2039–2045. <https://doi.org/10.1007/s10967-017-5171-8>
- Chmeleff, J., vonBlanchenburg, F., Kossert, K., & Jakob, D. (2010). Determination of the <sup>10</sup>Be half-life by multicollector ICP-MS and liquid scintillation counting. *Nuclear Instruments and Methods in Physics Research B*, 263(2), 192–199.
- Corbett, E., & Anderson, R. C. (2006). Landscape analysis of Illinois and Wisconsin Remnant Prairies. *Journal of the Torrey Botanical Society*, 133(2), 267–279. [https://doi.org/10.3159/1095-5674\(2006\)133\[267:LAOIAW\]2.0.CO;2](https://doi.org/10.3159/1095-5674(2006)133[267:LAOIAW]2.0.CO;2)
- De Alba, S., Lindstrom, M., Schumacher, T. E., & Malo, D. D. (2004). Soil landscape evolution due to soil redistribution by tillage: A new conceptual model of soil catena evolution in agricultural landscapes. *Catena*, 58(1), 77–100. <https://doi.org/10.1016/j.catena.2003.12.004>
- Dunai, T. J. (2010). *Cosmogenic nuclides: Principles, concept and applications in the Earth surface sciences*. Cambridge, UK, and New York: Cambridge University Press. <https://doi.org/10.1017/CBO9780511804519>
- Ebert, K., Willenbring, J. K., Norton, K. P., Hall, A., & Hattestrand, C. (2012). Meteoric <sup>10</sup>Be concentrations from saprolite and till in northern Sweden: Implications for glacial erosion and age. *Quaternary Geochronology*, 12, 11–22. <https://doi.org/10.1016/j.quageo.2012.05.005>

- Field, C. V., & Schmidt, G. A. (2009). Model-based constraints on interpreting 20th century trends in ice core  $^{10}\text{Be}$ . *Journal of Geophysical Research*, 114, D12110. <https://doi.org/10.1029/2008JD011217>
- Frost, C. C. (2000). Presettlement fire frequency regimes of the United States: a first approximation. In C. C. Frost (Ed.), *Studies in landscape ecology and presettlement Vegetation of the Southeastern United States* (chap. 4, pp. 163–197). Chapel Hill, NC: University of North Carolina.
- García-Ruiz, J. M., Beguería, S., Nadal-Romero, E., González-Hidalgo, J. C., Lana-Renault, N., & Sanguin, Y. (2015). A meta-analysis of soil erosion rates across the world. *Geomorphology*, 239, 160–173. <https://doi.org/10.1016/j.geomorph.2015.03.008>
- Gardner, T. W., Jorgensen, D. W., Shuman, C., & Lemieux, C. R. (1987). Geomorphic and tectonic process rates: Effects of measured time interval. *Geology*, 15(3), 259–261. [https://doi.org/10.1130/0091-7613\(1987\)15<259:GATPRE>2.0.CO;2](https://doi.org/10.1130/0091-7613(1987)15<259:GATPRE>2.0.CO;2)
- Gocke, M., Pustovoytov, K., & Kuzyakov, Y. (2010). Effect of  $\text{CO}_2$  concentration on the initial recrystallization rate of pedogenic carbonate—Revealed by  $^{14}\text{C}$  and  $^{13}\text{C}$  labeling. *Geoderma*, 155(3–4), 351–358. <https://doi.org/10.1016/j.geoderma.2009.12.018>
- Govers, G., Giménez, R., & van Oost, K. (2007). Rill erosion: Exploring the relationship between experiments, modelling and field observations. *Earth-Science Reviews*, 84(3–4), 87–2102. <https://doi.org/10.1016/j.earscirev.2007.06.001>
- Graly, J. A., Bierman, P. R., Ruessler, L. J., & Pavich, M. J. (2010). Meteoric  $^{10}\text{Be}$  in soil profiles – A global meta-analysis. *Geochimica et Cosmochimica Acta*, 74(23), 6814–6829. <https://doi.org/10.1016/j.gca.2010.08.036>
- Graly, J. A., Ruessler, L. J., & Bierman, P. R. (2011). Short and long-term delivery rates of meteoric  $^{10}\text{Be}$  to terrestrial soils. *Earth and Planetary Science Letters*, 302(3–4), 329–336. <https://doi.org/10.1016/j.epsl.2010.12.020>
- Granger, S., & Kelly, S. (2005). Historic Context Study of Minnesota Farms, 1820–1960. Minnesota Department of Transportation Work Order #13. Available online. <https://www.dot.state.mn.us/culturalresources/farmsteads.html>. Accessed 28-DEC-2017.
- Harden, J. W., Fries, T. L., & Pavich, M. J. (2002). Cycling of beryllium and carbon through hillslope soils in Iowa. *Biogeochemistry*, 60(3), 317–336. <https://doi.org/10.1023/A:1020308729553>
- Harris, K. L. (2003). *Geologic atlas of Pope County, Minnesota*. Minneapolis, Minnesota: Minnesota Geological Survey.
- Hassouni, K., & Bouhlassa, S. (2006). Estimation of soil erosion on cultivated soils using  $^{137}\text{Cs}$  measurements and calibration models: A case study from Nakhla watershed, Morocco. *Canadian Journal of Soil Science*, 86(1), 77–87. <https://doi.org/10.4141/S04-052>
- He, Q., & Walling, D. E. (1996). Interpreting particle size effects in the adsorption of  $^{137}\text{Cs}$  and unsupported  $^{210}\text{Pb}$  by mineral soils and sediments. *Journal of Environmental Radioactivity*, 30(2), 117–137. [https://doi.org/10.1016/0265-931X\(96\)89275-7](https://doi.org/10.1016/0265-931X(96)89275-7)
- Heikkilä, U., Beer, J., Are, J. A., & Steinhilber, F. (2013). On the atmospheric transport and deposition of the cosmogenic radionuclides ( $^{10}\text{Be}$ ): A review. *Space Science Reviews*, 176(1–4), 321–332. <https://doi.org/10.1007/s11214-011-9838-0>
- Heikkilä, U., Beer, J., & Feichter, J. (2008). Modeling cosmogenic radionuclides  $^{10}\text{Be}$  and  $^7\text{Be}$  during the Maunder minimum using the ECHAM5–HAM general circulation model. *Atmospheric Chemistry and Physics*, 8(10), 2797–2809. <https://doi.org/10.5194/acp-8-2797-2008>
- Heikkilä, U., Shi, X., Phipps, S. J., & Smith, A. M. (2014).  $^{10}\text{Be}$  in late deglacial climate simulated by ECHAM5–HAM—Part 2: Isolating the solar signal from  $^{10}\text{Be}$  deposition. *Climate of the Past*, 10(2), 687–696. <https://doi.org/10.5194/cp-10-687-2014>
- IUSS Working Group WRB (2015). World reference base for soil resources 2014, update 2015 International soil classification system for naming soils and creating legends for soil maps. World Soil Resources Reports no. 106. FAO, Rome.
- Jagercikova, M., Cornu, S., Bourles, D., Evrard, O., Hatte, C., & Balesdent, J. (2017). Quantification of a vertical solid matter transfers in soils during pedogenesis by a multi-tracer approach. *Journal of Soils and Sediments*, 17(2), 408–422. <https://doi.org/10.1007/s11368-016-1560-9>
- Jelinski, N. A., & Yoo, K. (2016). The distribution and genesis of eroded phase soils in the conterminous United States. *Geoderma*, 279, 149–164. <https://doi.org/10.1016/j.geoderma.2016.05.015>
- Johnson, M. O., Mudd, S. M., Pillars, B., Spooner, N. A., Fifield, L. K., Kirkby, M. J., & Goor, M. (2014). Quantifying the rate and depth dependence of bioturbation based on optically-stimulated luminescence (OSL) dates and meteoric  $^{10}\text{Be}$ . *Earth Surface Processes and Landforms*, 39(9), 1188–1196. <https://doi.org/10.1002/esp.3520>
- Kaste, J. M., Heimsath, A. M., & Bostick, B. C. (2007). Short-term soil mixing quantified with fallout radionuclides. *Geology*, 35(3), 243–246. <https://doi.org/10.1130/G23355A.1>
- Kaste, J. M., Heimsath, A. M., & Hohmann, M. (2006). Quantifying sediment transport across an undisturbed prairie landscape using cesium-137 and high resolution topography. *Geomorphology*, 76(3–4), 430–440. <https://doi.org/10.1016/j.geomorph.2005.12.007>
- Kirkby, M. J. (1985). A basis for soil profile modelling in a geomorphic context. *Journal of Soil Science*, 36(1), 97–121. <https://doi.org/10.1111/j.1365-2389.1985.tb00316.x>
- Konert, M., & Vandenberghe, J. (1997). Comparison of laser grain size analysis with pipette and sieve analysis: A solution for the underestimation of the clay fraction. *Sedimentology*, 44(3), 523–535. <https://doi.org/10.1046/j.1365-3091.1997.d01-38.x>
- Korschinek, G., Bergmaler, A., Dillman, I., Faestermann, T., Gerstmann, U., Knie, K., & Gostomski, C. L. (2009). Determination of the  $^{10}\text{Be}$  half-life by HI-ERD and liquid scintillation counting. *Geochimica et Cosmochimica Acta*, 73, A685–A685.
- Lal, D. (1991). Cosmic ray labeling of erosion surfaces: In situ nuclide production rates and erosion models. *Earth and Planetary Science Letters*, 104(2–4), 424–439. [https://doi.org/10.1016/0012-821X\(91\)90220-C](https://doi.org/10.1016/0012-821X(91)90220-C)
- Lal, R., Fifield, K., Time, S. G., Wassen, R. J., & Howe, D. (2012). A study of soil formation rates using  $^{10}\text{Be}$  in the wet-dry tropics of northern Australia. EPJ Web of Conferences 35, 01001. <https://doi.org/10.1051/epjconf/20123501001>
- Lal, R., & Stewart, B. A. (2012). Sustainable Management of Soil Resources and Food Security. In R. Lal, & B. A. Stewart (Eds.), *World soil resources and food security. Advances in soil science* (Vol. 18, chap. 1, pp. 1–10). Boca Raton, FL: CRC Press.
- Lepper, K., Fisher, T. G., Hajdas, I., & Lowell, T. (2007). Ages for the Big Stone Moraine and the oldest beaches of glacial Lake Agassiz: Implications for deglaciation chronology. *Geology*, 35(7), 667–670. <https://doi.org/10.1130/G23665A.1>
- Li, S., Lobb, D. A., Lindstrom, M. J., & Fahrenhorst, A. (2007). Tillage and water erosion on different landscapes in the northern North American Great Plains evaluated using  $^{137}\text{Cs}$  technique and soil erosion models. *Catena*, 70(3), 493–505. <https://doi.org/10.1016/j.catena.2006.12.003>
- Li, S., Lobb, D. A., Lindstrom, M. J., Papiernik, S. K., & Fahrenhorst, A. (2008). Modeling tillage-induced redistribution of soil mass and its constituents within different landscapes. *Soil Science Society of America Journal*, 72(1), 167–179. <https://doi.org/10.2136/sssaj2006.0418>
- Li, S., Lobb, D. A., Tiessen, K. H., & McConkey, B. G. (2010). Selecting and applying cesium-137 conversion models to estimate soil erosion rates in cultivated fields. *Journal of Environmental Quality*, 39(1), 204–219. <https://doi.org/10.2134/jeq2009.0144>
- Lin, H., Wheeler, D., Bell, J., & Wilding, L. (2005). Assessment of soil spatial variability at multiple scales. *Ecological Modeling*, 182(3–4), 271–290. <https://doi.org/10.1016/j.ecolmodel.2004.04.006>
- Mayer, L. M., & Xing, B. (2001). Organic matter–surface area relationships in acid soils. *Soil Science Society of America Journal*, 65(1), 250–258. <https://doi.org/10.2136/sssaj2001.651250x>

- Mikhailova, E. A., & Post, C. J. (2006). Effects of land use on soil inorganic carbon stocks in the Russian Chernozem. *Journal of Environmental Quality*, 35(4), 1384–1388. <https://doi.org/10.2134/jeq2005.0151>
- Minnesota County Biological Survey (2003). *Native plant communities and rare species in Pope County, Minnesota*. St. Paul, MN: State of Minnesota Department of Natural Resources. <https://files.dnr.state.mn.us/eco/mcbs/maps/pope.pdf>
- Minnesota Department of Natural Resources Staff (1988). Natural vegetation of Minnesota at the Time of the public land Survey: 1847-1907. Biological Report No. 1.6 pp.
- Monaghan, M. C., McKean, J., Dietrich, W. E., & Klein, J. (1992).  $^{10}\text{Be}$  chronometry of bedrock-to-soil conversion rates. *Earth and Planetary Science Letters*, 111(2-4), 483–492. [https://doi.org/10.1016/0012-821X\(92\)90198-5](https://doi.org/10.1016/0012-821X(92)90198-5)
- Montgomery, D. R. (2007). Soil erosion and agricultural sustainability. *Proceedings of the National Academy of Sciences of the United States of America*, 104(33), 13,628–13,272.
- Nash, J. E., & Sutcliffe, J. V. (1970). River flow forecasting through conceptual models, part I — A discussion of principles. *Journal of Hydrology*, 10(3), 282–290. [https://doi.org/10.1016/0022-1694\(70\)90255-6](https://doi.org/10.1016/0022-1694(70)90255-6)
- National Cooperative Soil Survey (NCSS) (2017). National Cooperative Soil Survey Characterization Database. <https://ncsslabsdatamart.sc.egov.usda.gov/>. Accessed Thursday, December 21, 2017
- Nearing, M. A., Xie, Y., Liu, B., & Ye, Y. (2017). Natural and anthropogenic rates of soil erosion. *International Soil and Water Conservation Research*, 5(2), 77–84. <https://doi.org/10.1016/j.iswcr.2017.04.001>
- Nishiizumi, K., Imamura, M., Caffee, M., Southon, J. R., Finkel, R. C., & McAninch, J. (2007). Absolute calibration of  $^{10}\text{Be}$  AMS standards. *Nuclear Instruments and Methods in Physics Research Section B*, 258(2), 403–413. <https://doi.org/10.1016/j.nimb.2007.01.297>
- Papiernik, S. K., Lindstrom, M. J., Schumacher, J. A., Farenhorst, A., Stephens, K. D., Schumacher, T. E., & Lobb, D. A. (2005). Variation in soil properties and crop yield across an eroded prairie landscape. *Journal of Soil and Water Conservation*, 60(6), 388–395.
- Papiernik, S. K., Lindstrom, M. J., Schumacher, T. E., Schumacher, J. A., Malo, D. D., & Lobb, D. A. (2007). Characterization of soil profiles in a landscape affected by long-term tillage. *Soil and Tillage Research*, 93(2), 335–345. <https://doi.org/10.1016/j.still.2006.05.007>
- Parsons, A. J., & Foster, I. D. L. (2011). What can we learn about soil erosion from the use of  $^{137}\text{Cs}$ ? *Earth-Science Reviews*, 108(1-2), 101–113. <https://doi.org/10.1016/j.earscirev.2011.06.004>
- Pavich, M. J., Brown, L., Harden, J. W., Klein, J., & Middleton, R. (1986).  $^{10}\text{Be}$  distribution in soils from Merced River terraces, California. *Geochimica et Cosmochimica Acta*, 50(8), 1727–1735. [https://doi.org/10.1016/0016-7037\(86\)90134-1](https://doi.org/10.1016/0016-7037(86)90134-1)
- Pavich, M. J., Brown, L., & Vallette-Silver, J. N. (1985).  $^{10}\text{Be}$  analysis of a quaternary weathering profile in the Virginia Piedmont. *Geology*, 1(1), 39–41.
- Portenga, E. W., Bishop, P., Rood, D. H., & Bierman, P. R. (2017). Combining bulk sediment OSL and meteoric  $^{10}\text{Be}$  fingerprinting techniques to identify gully initiation sites and erosion depths. *Journal of Geophysical Research: Earth Surface*, 122, 513–527. <https://doi.org/10.1002/2016JF004052>
- Porto, P., Walling, D. E., Tamburino, V., & Callegari, G. (2003). Relating caesium-137 and soil loss from cultivated land. *Catena*, 53(4), 303–326. [https://doi.org/10.1016/S0341-8162\(03\)00084-5](https://doi.org/10.1016/S0341-8162(03)00084-5)
- Quine, T. A., & van Oost, K. (2007). Quantifying carbon sequestration as a result of soil erosion and deposition: Retrospective assessment using caesium-137 and carbon inventories. *Global Change Biology*, 13(12), 2610–2625. <https://doi.org/10.1111/j.1365-2486.2007.01457.x>
- Rahaman, W., Wittman, H., & von Blanckenburg, F. (2017). Denudation rates and the degree of chemical weathering in the Ganga River basin from ratios of meteoric cosmogenic  $^{10}\text{Be}$  to stable  $^9\text{Be}$ . *Earth and Planetary Science Letters*, 469, 156–169. <https://doi.org/10.1016/j.epsl.2017.04.001>
- Ramankutty, N., & Foley, J. A. (1999). Estimating historical changes in land cover: North American croplands from 1850-1992. *Global Ecology and Biogeography*, 8(5), 381–396. <https://doi.org/10.1046/j.1365-2699.1999.00141.x>
- Renard, K., Foster, G., Weesies, G., McCool, D., & Yoder, D. (1997). *Predicting soil erosion by water: A guide to conservation planning with the Revised Universal Soil Loss Equation (RUSLE)*. Washington, DC: US Government Printing Office.
- Retallack, G. J. (2005). Pedogenic carbonate proxies for amount and seasonality of precipitation in paleosol. *Geology*, 33(4), 333–336. <https://doi.org/10.1130/G21263.1>
- Reusser, L. J., & Bierman, P. R. (2010). Using meteoric  $^{10}\text{Be}$  to track fluvial sand through the Waipaoa River basin, New Zealand. *Geology*, 38(1), 47–50. <https://doi.org/10.1130/G30395.1>
- Roering, J. J., Kirchner, J. W., & Dietrich, W. E. (1999). Evidence for nonlinear, diffusive sediment transport on hillslopes and implications for landscape morphology. *Water Resources Research*, 35(3), 853–870. <https://doi.org/10.1029/1998WR900090>
- Sadler, P. M. (1981). Sediment accumulation and the completeness of stratigraphic sections. *Journal of Geology*, 89(5), 569–584. <https://doi.org/10.1086/628623>
- Sadler, P. M. (1994). The expected duration of upward-shallowing carbonate cycles and their terminal hiatuses. *Geological Society of America Bulletin*, 106(6), 791–802. [https://doi.org/10.1130/0016-7606\(1994\)106<0791:TEDOUS>2.3.CO;2](https://doi.org/10.1130/0016-7606(1994)106<0791:TEDOUS>2.3.CO;2)
- Sanford, W. E., & Selznick, D. L. (2013). Estimation of evapotranspiration across the conterminous United States using a regression with climate and land-cover data. *Journal of the American Water Resources Association*, 49(1), 217–230. <https://doi.org/10.1111/jawr.12010>
- Schoeneberger, P. J., Wysocki, D. A., & Benham, E. C. (Eds.) (2011). *Field book for describing and sampling the soil*, Version 3.0. Natural Resources Conservation Service, National Soil Survey Center, Lincoln, NE.
- Schoonejans, J., Vanacker, V., Opfergelt, S., & Christl, M. (2017). Long-term soil erosion derived from in-situ  $^{10}\text{Be}$  and inventories of meteoric  $^{10}\text{Be}$  in deeply weathered soils in southern Brazil. *Chemical Geology*, 466, 380–388. <https://doi.org/10.1016/j.chemgeo.2017.06.025>
- Schumacher, J. A., Kaspar, T. C., Ritchie, J. C., Schumacher, T. E., Karlen, D. L., Venteris, E. R., et al. (2005). Identifying spatial patterns of erosion for use in precision conservation. *Journal of Soil and Water Conservation*, 60(6), 355–362.
- Soil Survey Staff, Natural Resources Conservation Service, United States Department of Agriculture (2014). *Keys to soil taxonomy*, (12th ed.). Washington, DC: USDA-Natural Resources Conservation Service.
- Soil Survey Staff, Natural Resources Conservation Service, United States Department of Agriculture (2017). Soil Survey Geographic (SSURGO) Database for Pope County, Minnesota. Available online. Accessed 12-20-2017.
- Tester, J. R. (1995). Tallgrass Prairie. In J. R. Tester (Ed.), *Minnesota's natural heritage: An ecological perspective* (chap. 6, pp. 121–160). Minneapolis, MN: University of Minnesota Press.
- Tsai, H., Maejima, Y., & Hseu, Z.-Y. (2008). Meteoric  $^{10}\text{Be}$  dating of highly weathered soils from fluvial terraces in Taiwan. *Quaternary International*, 188(1), 185–196. <https://doi.org/10.1016/j.quaint.2007.06.007>
- Tuo, D., Xu, M., & Gao, G. (2018). Relative contributions of wind and water erosion to total soil loss and its effect on soil properties in sloping croplands of the Chinese Loess Plateau. *Science of the Total Environment*, 633, 1032–1040. <https://doi.org/10.1016/j.scitotenv.2018.03.237>

- U.S. Department of the Interior, Bureau of Land Management (2017). General land office records. Available online. <https://glorerecords.blm.gov>. Accessed 28-DEC-2017.
- University of Minnesota, John R. Borchert Map Library (2017). Minnesota historical aerial photographs online. Accessed 12-20-2017. <https://www.lib.umn.edu/apps/mhapo/>
- van der Meij, W. M., Temme, A. J. A. M., Wallinga, J., Hierold, W., & Sommer, M. (2017). Topography reconstruction of eroding landscapes—A case study from a hummocky ground moraine (CarboZALF-D). *Geomorphology*, *295*, 758–772. <https://doi.org/10.1016/j.geomorph.2017.08.015>
- van Oost, K., Govers, G., & Desmet, P. (2000). Evaluating the effects of changes in landscape structure on soil erosion by water and tillage. *Landscape Ecology*, *15*(6), 577–589. <https://doi.org/10.1023/A:1008198215674>
- van Oost, K., van Muysen, W., Govers, G., Heckrath, G., Quine, T. A., & Poesen, J. (2003). Simulation of the redistribution of soil by tillage on complex topographies. *European Journal of Soil Science*, *54*(1), 63–76. <https://doi.org/10.1046/j.1365-2389.2003.00470.x>
- van Oost, K., Verstraeten, G., Doetterl, S., Notebaert, B., Wiaux, F., Broothaerts, N., & Six, J. (2012). Legacy of human-induced C erosion and burial on soil-atmosphere C exchange. *Proceedings of the National Academy of Sciences of the United States of America*, *109*(47), 19,492–19,497. <https://doi.org/10.1073/pnas.1211162109>
- Veenstra, J. J., & Burras, C. L. (2012). Effects of agriculture on the classification of Black soils in the Midwestern United States. *Canadian Journal of Soil Science*, *92*(3), 403–411. <https://doi.org/10.4141/cjss2010-018>
- Višnjić, V., Frédéric, H., & Podladchikov, Y. (2018). Reconstructing spatially variable mass balances from past ice extents by inverse modeling. *Journal of Glaciology*, *64*(248), 957–968. <https://doi.org/10.1017/jog.2018.82>
- von Blanckenburg, F., Bouchez, J., & Wittmann, H. (2012). Earth surface erosion and weathering from the  $^{10}\text{Be}$  (meteoric)/ $^9\text{Be}$  ratio. *Earth and Planetary Science Letters*, *351*–352, 295–305. <https://doi.org/10.1016/j.epsl.2012.07.022>
- Wagai, R., Mayer, L. M., & Kitayama, K. (2009). Extent and nature of organic coverage of soil mineral surfaces assessed by a gas sorption approach. *Geoderma*, *149*(1–2), 152–160. <https://doi.org/10.1016/j.geoderma.2008.11.032>
- Walling, D.E., & He, Q. (2001). Model for converting  $^{137}\text{Cs}$  measurements to estimates of soil redistribution on cultivated and uncultivated soils, and estimating bomb-derived  $^{137}\text{Cs}$  reference inventory (Including Software for Model Implementation). A contribution to the International Atomic Energy Agency Coordinated Research Programmes on Soil Erosion (D1.50.05) and Sedimentation (F3.10.01). Dep. of Geography, Exeter, UK.
- Walling, D. E., He, Q., & Appleby, P. C. (2002). Conversion models for use in soil-erosion, soil-redistribution, and sedimentation investigations. In F. Zapata (Ed.), *Handbook for the assessment of soil erosion and sedimentation using environmental radioactivity* (pp. 111–164). Dordrecht, the Netherlands: Kluwer Academic Publ.
- West, N., Kirby, E., Bierman, P., Slingerland, R., Ma, L., Rood, D., & Brantley, S. (2013). Re- golith production and transport at the Susquehanna Shale Hills Critical Zone Observatory. Part 2: Insights from meteoric  $^{10}\text{Be}$ . *Journal of Geophysical Research: Earth Surface*, *118*, 1877–1896. <https://doi.org/10.1002/jgrf.20121>
- Western Regional Climate Center (2017). Cooperative climatological data summaries. Retrieved from <https://wrcc.dri.edu/climatedata/climsum/>
- Willenbring, J. K., & von Blanckenburg, F. (2010). Meteoric cosmogenic beryllium-10 adsorbed to river sediment and soil: Applications for earth surface dynamics. *Earth Science Reviews*, *98*(1–2), 105–122. <https://doi.org/10.1016/j.earscirev.2009.10.008>
- Wittman, H., & von Blanckenburg, F. (2016). The geological significance of cosmogenic nuclides in large lowland river basins. *Earth Science Reviews*, *159*, 118–141. <https://doi.org/10.1016/j.earscirev.2016.06.001>
- Wittmann, H., von Blanckenburg, F., Dannhaus, N., Bouchez, J., Guyot, J. L., Maurice, L., et al. (2015). A test of the new cosmogenic  $^{10}\text{Be}$ (meteoric)/ $^9\text{Be}$  proxy for simultaneously determining basin-wide erosion rates, denudation rates, and the degree of weathering in the Amazon basin. *Journal of Geophysical Research: Earth Surface*, *120*, 2498–2528.
- Wright, H. E. (1962). Role of the Wadena lobe in the Wisconsin glaciation of Minnesota. *Geological Society of America Bulletin*, *73*(1), 73–100. [https://doi.org/10.1130/0016-7606\(1962\)73\[73:ROTWLI\]2.0.CO;2](https://doi.org/10.1130/0016-7606(1962)73[73:ROTWLI]2.0.CO;2)
- Yaalon, D. H. (1983). Climate, Time and Soil Development. In L. P. Wilding, N. E. Smeck, & G. F. Hall (Eds.), *Pedogenesis and soil taxonomy I. Concepts and interactions. Developments in soil science 11A* (chap. 8, pp. 233–252). Amsterdam: Elsevier.
- Zhang, X. C., Zhang, G. H., & Wei, X. (2015). How to make  $^{137}\text{Cs}$  erosion estimation more useful: An uncertainty perspective. *Geoderma*, *239*–240, 186–194. <https://doi.org/10.1016/j.geoderma.2014.10.004>